Detection of a Divot in the Size Distribution of the Kuiper Belt's Scattering Objects

by

Cory Jason Shankman

B.Sc., The University of Western Ontario, 2010

A THESIS SUBMITTED IN PARTIAL FULFILMENT OF
THE REQUIREMENTS FOR THE DEGREE OF

MASTER OF SCIENCE

in

The Faculty of Graduate Studies

(Astronomy)

THE UNIVERSITY OF BRITISH COLUMBIA
(Vancouver)

August 2012

Abstract

We present a joint analysis of the Canada France Ecliptic Plane Survey's scattering objects, and the Kaib et al. (2011b) orbital model, measuring the scattering objects' size distribution. Scattering objects are Trans-Neptunian objects which are strongly interacting with Neptune, having scattering encounters which change their semimajor axes on short dynamical timescales. We reject a single power-law distribution at the 99% level, and find that a dearth of small objects is required. We present a novel parameterisation of a divot size distribution, which rises as a single power-law to a precipitous drop, then recovers as another single power-law of potentially different slope. We constrain the form of such a divot distribution, and find that divots are preferred over "knee" size distributions, which are found elsewhere in the literature for different populations. We present our preferred divot scenario, which rises as a single power-law of logarithmic slope $\alpha = 0.8$ as absolute H_g magnitudes increase to sizes corresponding to $D \sim 100$ km, then dropping by a factor of about 6 in differential number, followed by another single power-law of logarithmic slope $\alpha = 0.5$. Our interpretation is that this feature arose from the size distribution made by planetesimal formation and is now "frozen in" to the "hot" populations of the outer Solar System. From this we estimate there are $2 \cdot 10^9$ scattering objects with $H_g < 18$, allowing for enough to supply the nearby Jupiter Family comets. This interpretation nicely ties the "hot" populations together while simultaneously explaining the source of the Jupiter Family comets and the observed paucity of intermediate-sized (50-100 km) Neptune Trojans.

Preface

- Identification and design of research project: Measuring the size distribution of the Canada France Ecliptic Plane Survey scattering objects was a project suggested to the author by Brett Gladman. The form of the candidate size distributions were determined by both Brett Gladman and the author.

- Performing the research: the author inherited the Canada France Ecliptic Plane Survey's survey simulator from work by Jean-Marc Petit and J.J. Kavelaars, and modified it to accept several candidate size distribution formulations. Additionally, the simulator was modified by the author for easy deployment of a grid search on a computing cluster. An orbital model, modified with input from Brett Brett Gladman and the author, was provided by Dr. Nathan Kaib. The author extracted the scattering object sample from the provided orbital model. A code for determining the Anderson-Darling statistic was inherited from Samantha Lawler. Possible candidate size distributions were explored by the author, with input from Brett Gladman, which is the subject of this work.

- Manuscript preparation: This manuscript was written entirely by the author, with feedback from Brett Gladman. The work presented in this manuscript has been submitted for publication. Section 4.6.2 was adapted from the submitted work.

Table of Contents

List of Tables

List of Figures

Glossary

Acronym/Symbol	Definition
a	semimajor axis
e	eccentricity
i	inclination
d	heliocentric distance at detection
H_g	absolute magnitude in g-band
AU	astronomical unit
JFC	Jupiter-family comet
P	orbital period
q	perihelion distance
D	diameter
n	diameter distribution power-law index
p	albedo
α	H distribution logarithmic "slope"
TNO	Trans-Neptunian Object
m	apparent magnitude
R	heliocentric distance
Δ	geocentric distance
r	radius
ρ	density
M	mass

Table 1: Glossary of acronyms and symbols.

Acknowledgements

I would like to thank my supervisor, Brett Gladman, for his guidance and patience. This work would not have been possible without your insight, intuition and expertise.

I would like to thank Brett Gladman, J.J. Kavelaars, Jean-Marc Petit and the rest of the Canada France Ecliptic Plane Survey team for their work in the survey. I would also like to thank Nathan Kaib for his modelling contributions. You all laid the necessary groundwork, enabling me to carry out this project.

To my mom, dad and brother: thank you for always being supportive of my endeavours.

Mike, Sam and Sarah: thank you for your help, and for being a sounding board. And thank you to all the Astronomy graduate students for being there to distract in between work sessions.

Thanks to Ingrid Stairs, who acted as second reader for this thesis and helped clarify several important points.

This work was funded by the University of British Columbia, the department of Physics and Astronomy, and the Natural Sciences and Engineering Research Council of Canada.

Chapter 1

The Outer Solar System

1.1 Introduction

The outer Solar System, beginning at Jupiter, encompasses the four giant planets and a variety of small-body populations. The outer extent reaches distances of tens of thousands of astronomical units[1] (AU) with the Oort Cloud. This work focuses on the directly observed populations, which only extend out to tens of AU. The small-body populations of the outer Solar System are, listed by distance: Jupiter Trojans, Jupiter Family Comets (JFCs), Centaurs [2], Neptune Trojans, the Kuiper Belt (which has sub-populations), and the scattering objects. All objects with a semimajor axis beyond that of Neptune's are generically referred to as Trans-Neptunian Objects (TNOs). A fundamental characteristic of all small-body populations in the Solar System is their size distribution. Chapter 1 covers the relevant background on the outer Solar System populations to understand the significance of a measured divot in the scattering population's size distribution.

1.2 Size Distributions

A key characteristic of small-body populations is the focus of this work: the size distribution. Some combination of accretional physics, which builds smaller objects, and collisional physics, which also preferentially produces smaller objects, imbues a population with a distinct distribution of sizes. Collisional and accretional theories suggest that the size distributions could take the form of a power-law diameter, D, distribution:

$$\frac{\mathrm{d}N}{\mathrm{d}D} \propto D^{-\mathrm{n}} \tag{1.1}$$

where the power-law index n is set by the history of the population. Collisional models, where the collisions are independent of the body's cohesive

[1] 1 AU is the mean Earth–Sun distance

[2] Objects on planet crossing orbits with a semimajor axis < 30 AU and pericentre < 7.5 AU that have not coupled with Jupiter.

strength, find that collisional evolution produces a power law of this form, with n= 3.5 (Dohnanyi, 1969). More recent detailed analytic and numerical work, taking into account the objects' strength, also find a power law with n near 3.5, depending on the conditions (O'Brien and Greenberg, 2005). This slope is referred to as the collisional equilibrium slope; populations which have evolved collisionally should tend towards a slope of this value. Accretional simulations build a size distribution as in Equation 1.1, with the n value dependent on the initial conditions of the Solar nebula. The most recent accretional simulations find a size distribution with n $\simeq$ 5 (Kenyon and Bromley, 2012). The size distribution provides access to the population's formative and collisional processes, and thus help constrain the conditions of the early Solar System.

For most observation techniques, the diameters of TNOs are not directly measurable; it is only possible to get a diameter by assuming an albedo [3], p. To avoid this, many astronomers instead use the observable magnitude or the absolute magnitude [4], H to measure the size distribution. The power-law D distribution corresponds to the exponential H distribution[5].

$$\frac{\mathrm{d}N}{\mathrm{d}H} \propto 10^{\alpha H} \tag{1.2}$$

where α is the logarithmic "slope" and maps to the power-law n value (n = $5\alpha+1$). Equation 1.2 is easily rewritten to emphasise that α is a logarithmic "slope", with k being an unspecified constant:

$$\log N = k + \alpha \cdot H \tag{1.3}$$

The slope α is commonly measured from a distribution of magnitudes (as with a cumulative luminosity function), but Solar System surveys are done with reflected light, and so highly sensitive to distance, which an apparent magnitude distribution does not take into account. Ignoring information about the distance of detection, d, can obscure features in the size distribution. Another source for error arises when the results from multiple surveys are combined; often the observational biases of the particular surveys can not be taken fully into account when combined. This work avoids both of

[3] Diameters can be found from the observable H_g and the albedo p: $D = 100 \text{ km } \sqrt{0.05/p}\, 10^{0.2(9.16-H_g)}$.

[4] $H = < m > +2.5 \log \frac{\phi(\gamma)}{\Delta^2 R^2}$, with $< m >$, average apparent magnitude, R, heliocentric distance, $\phi(\gamma)$, a phase factor of order unity, and Δ, geocentric distance.

[5] Measuring a distribution of H magnitudes is a proxy for the D distribution, and so is also called a size distribution. Henceforth in this work the term "size distribution" refers to the H distribution.

these pitfalls by exclusively using H magnitudes measured in g-band and observations from the well characterised Canada France Ecliptic Plane Survey (CFEPS, see Section 2.1).

Slopes[6] have been measured throughout the Solar System and it is found that single power-law forms generally fit well over ranges of a few magnitudes. Measurements exist for the main belt asteroids, near Earth objects, saturnian ring system, Jupiter Trojans, Jupiter Family Comets (JFCs), and the Kuiper Belt. Slopes for the inner Solar System populations are generally found to be shallow (0.3-0.5) (Bottke et al., 2002; Gladman et al., 2009; Jedicke et al., 2002) and outer Solar System populations have steeper slopes (0.8-1.2) (Elliot et al., 2005; Gladman et al., 2012; Petit et al., 2011). The distinct difference between these populations arises from their collisional histories. Inner Solar System objects have shorter period orbits and are more densely packed, and thus have been more collisionally eroded, leading to a shallower slope in their size distributions. The outer Solar System populations have undergone less collisional grinding; their steep slopes are presumably a signature of the formation conditions for the outer parts of the Solar System. These steep slopes cannot continue indefinitely, as the mass for an $\alpha > 0.6$ slope diverges as $H \to \infty$ ($D \to 0$, see Section 2.2.1 for proof); a change in form of the size distribution, which is generically called a break, is required. There is evidence for a break in the TNO populations (Bernstein et al., 2004; Fraser and Kavelaars, 2008; Fuentes and Holman, 2008), which is modelled as a sharp (a "knee"), or gradual ("rollover"), transition to a different single power-law.

This work examines three types of size distributions: single power-law, "knee", and a novel divot size distribution. Figure 1.1 shows schematics and parameters for these three distributions. The single power-law is simply parameterised by the slope α, as is shown in Equation 1.2. Both the "knee" and divot cases are two single power laws joined in some fashion at a specific H magnitude. Each is parameterised with a bright, α_b, and faint, α_f slope. Some works in the literature use a rolling power-law, which is a smoothed "knee"; these are not considered in this work as the sample size prevents a fine delineation between a "knee" and a rolling power-law. Divots have an extra parameter: the contrast, c, which is the ratio of the differential number on the bright side of the divot to the faint side. A larger value for c means a bigger drop across the divot. A "knee" can be thought of as a special case of the divot parameterisation, with $c = 1$.

This work is the first to model the size distribution with a divot. This

[6] Henceforth "slope" refers to an α value, which is a logarithmic "slope".

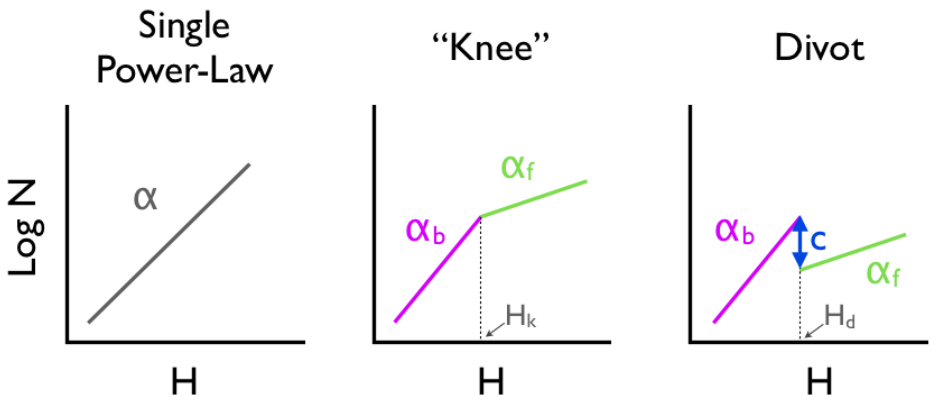

Figure 1.1: Schematics for the three size distributions considered in this work. The single power law is parameterised by its slope, α. Both the divot and "knee" are parameterised by a bright and faint slope, α_b and α_f respectively, and have a break H magnitude. Additionally, the divot has a contrast c, which increases for a larger drop; $c = 1$ gives a "knee".

size distribution is a key result of this work and essential for explaining several mysteries in the outer Solar System. Section 2.2 covers the the parameterisation of the divot distribution in greater detail.

It is no surprise that the size distribution might deviate from a single power-law. Figure 1.2 shows the size distribution for the main asteroid belt, which has several features. The main asteroid belt's size distribution is well-known, as surveys of the belt can see down to small sizes with great completeness. The size distribution in the asteroid belt differs from those in the outer Solar System, as the asteroid belt is much denser, with higher dispersion velocities, and thus collisional evolution plays a dominant role. The steeper slope from $H = 6 - 8$ may be accretional (Morbidelli et al., 2009); this result bears some uncertainty as it is based on < 100 asteroids. Additionally, accretional physics may have been different in the inner and outer Solar System. Section 1.3 covers the details of the measured size distributions for the outer Solar System populations.

In summary:

- Solar System small body populations have size distributions which arise from accretional and collisional processes.
- The outer Solar System populations have steep size distributions because they have not been significantly collisionally eroded post the

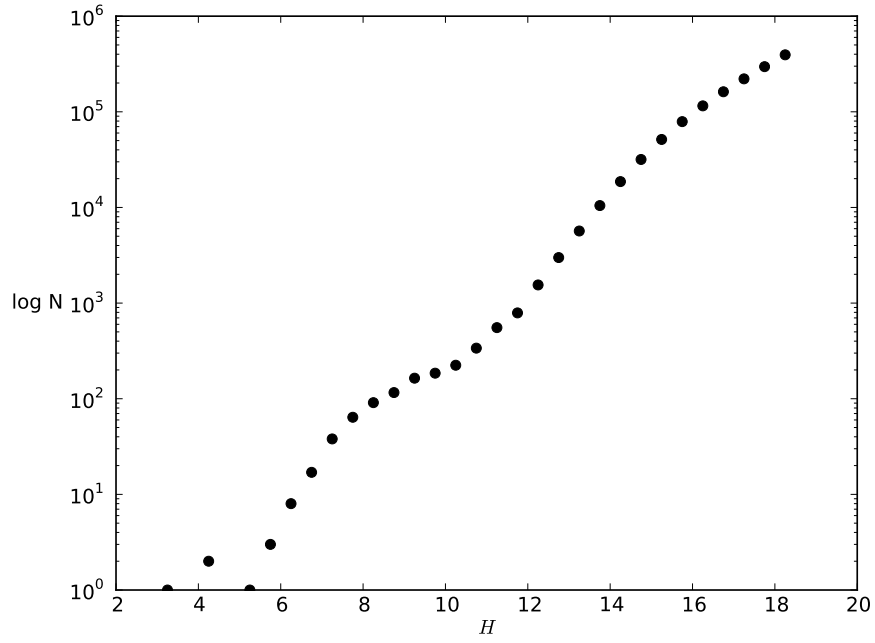

Figure 1.2: A representation of the main asteroid belt's differential H distribution, from a parametric representation by Jedicke et al. (2002). Data interpreted from Bottke et al. (2005). For reference H_g of 19 corresponds to $D \sim 1$ km and $H_g = 14$ to $D \sim 10$ km. The bump at the large-size end results from small number statistics.

epoch of planet building.

- These steep slopes cannot continue indefinitely. Additionally, there is evidence that they break.
- By studying the size distributions of the primordial TNO populations, we can gain access to and perhaps constrain the conditions at the time of Solar System formation.

1.3 Populations of the Outer Solar System

The small-body populations of the inner Solar System have have been well observed, with all large asteroid belt objects having been found. While

strong observational biases and great distances make it much harder to observe the outer Solar System populations, many small bodies have been observed, coming from several different populations (Fig. 1.4). The literature is rich with details about these populations, but to understand this work one needs only focus on two aspects: the size distributions, and the difference between the dynamically "hot" and "cold" populations. Figure 1.4 shows the inclinations of the known outer Solar System bodies. It is easy to pick out by simple visual inspection that there is a group of low inclination, "cold", objects between 42 and 47 AU; the rest have an extended, "hot", inclination distribution. This section discusses the various "hot" populations and their size distributions, for comparison with the new measurement of the scattering objects' (a "hot" population) size distribution.

1.3.1 The Kuiper Belt

The Kuiper Belt is a group of small bodies extending from semimajor axis $a = 30$ AU to a sharp outer edge at approximately $a = 48$ AU. Also in this region of space are members of the resonant, scattering and detached populations. Figure 1.3 shows a projection onto the ecliptic plane of a synthetic model for all of these populations, with the clear drop off at around 50 AU. Figures 1.4 and 1.5 show the orbital distributions for the known objects in the region around the Kuiper Belt. It is apparent from Fig. 1.4 that there are two distinct classical belt (black open triangle) inclination populations: "hot" and "cold". The "cold" objects have a low inclination, i distribution peaking at around 2.5° and the "hot" objects have an extended i distribution which goes up to $\sim 35°$ (Brown, 2001; Petit et al., 2011). These groups, while primarily distinguished on their inclination distributions, also have distinct colours (Sheppard, 2010), and size distributions (Bernstein et al., 2004; Fraser and Kavelaars, 2009; Petit et al., 2011) suggesting that they are truly two different populations. Of particular interest here is the idea that the "cold" classical belt was formed in place, and the "hot" population was implanted over top of it (Petit et al., 2011; Wolff et al., 2012). For objects larger than $D \sim 150$ km, the "hot" population has $\alpha = 0.8$ and the "cold" $\alpha = 1.2$ (Petit et al., 2011). The steeper size distribution from the "cold" population suggests that it has not been significantly collisionally eroded, which is consistent with having formed in outer part of the Solar System, where the collisional timescale is higher.

The deepest Kuiper Belt surveys to date found that the size distribution for faint H (small size) objects is shallow (Bernstein et al., 2004; Fraser and Kavelaars, 2009). This is in contrast to measurements for larger objects,

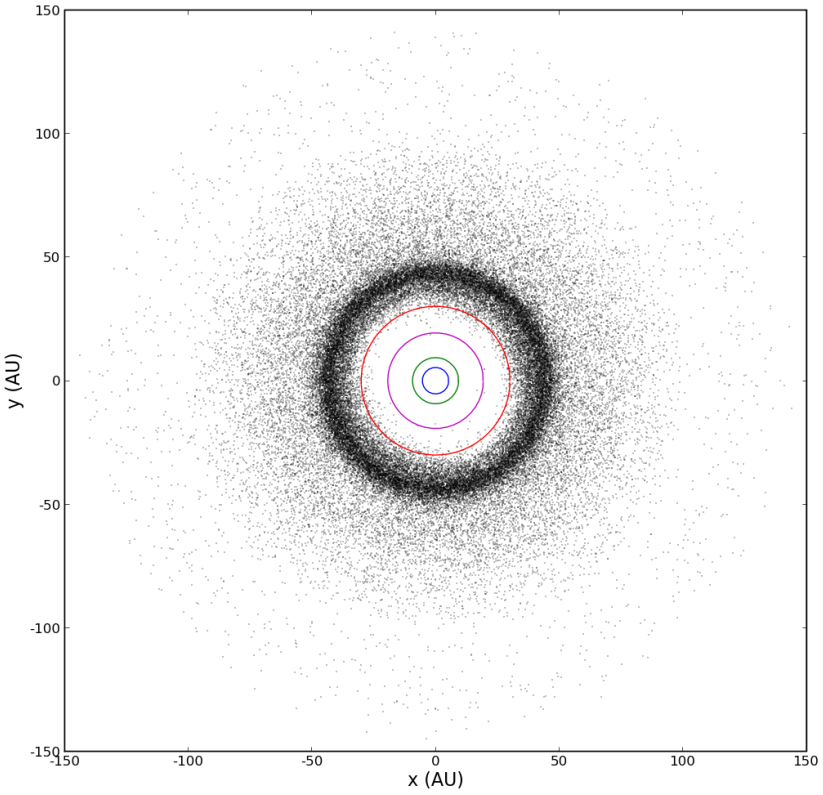

Figure 1.3: A plot of a synthetic model for the Kuiper Belt from a top-down view of the Solar System. The orbits of Jupiter, Saturn, Uranus and Neptune are overlayed. For details on the synthetic model see Petit et al. (2011). Synthetic distributions for the classical belt, scattering, detached and resonant objects are all plotted. Image courtesy of J.J. Kavelaars.

demonstrating that the size distribution breaks as expected. These measurements established the need for a broken power-law size distribution for the outer Solar System populations; there is no reason to believe the other outer Solar System populations would not also have broken power-laws.

Sprinkled across the Kuiper Belt region are the resonant populations, which inhabit mean-motion resonances with Neptune. TNOs are thought to have been captured in these resonances during the epoch when Neptune

migrated. In these resonances they are protected against close encounters with Neptune even with $q < 30$ AU (Fig 1.5 where they cross Neptune's orbit. Figure 1.4 shows that the resonant populations (open red squares) are also "hot". The Plutinos (the TNOs sharing Pluto's 3:2 resonance with Neptune) have a steep slope with $\alpha = 0.8 - 0.9$ (Gladman et al., 2012), which is consistent with the "hot" main Kuiper Belt. While there are issues of small sample sizes, and extreme observational biases to overcome, the observations to date are consistent with the notion that the "hot" objects in the Kuiper Belt share a common origin. Naturally one would want to extend this hypothesis to all of the "hot" populations in the outer Solar System, namely the scattering objects, Neptune Trojans, and JFCs. Linking all of the "hot" populations is a central strength of this work's main result.

1.3.2 Scattering Objects

The scattering/scattered objects are a set of TNOs whose orbital evolution is primarily driven interactions with Neptune (and hence have been/are being scattered). They are likely the close-in tail of a large population of objects which was scattered out of the early Solar System, and now forms the Oort Cloud (Duncan and Levison, 1997). The term "scattered disk" is historically used in the literature for scattered/scattering populations (Duncan and Levison, 1997; Trujillo et al., 2000), and its authors seek to define scattering objects via cuts in the orbital parameters, specifically a cut in the pericentre q. This approach focuses on the current location of an object, irrespective of its past or future orbital dynamics, and has several shortcomings. The simple q cut allows for the misclassification of resonant objects, and some inner main-belt TNOs, as scattered objects. Additionally, this classification scheme does not allow for differentiation in the cosmogony of an object, as only its current state is used.

We use the classification scheme from Gladman et al. (2008) to identify scattering objects based on dynamical criteria. Any TNO with semimajor axis $a < 2000$ AU whose a changes by 1.5 AU in a 10 Myr time-span is actively scattering. Table 2.1 lists the CFEPS scattering object sample (Petit et al., 2011), selected in this manner, which is used in this work.

Scattering objects occupy a much larger volume of the Solar System than any population interior to the Oort Cloud (see Fig. 1.4). Because they are being thrown about (scattered) by the Neptune and the other giant planets, they can simultaneously have large semimajor axes (100s of AU) and small pericentres, q, that come well inside Neptune, down to around 10 AU (Fig. 1.5). In a reflected light, flux-limited survey, distance is the key factor

in detectability. The close pericentre passages of scattering objects presents a great opportunity for measuring the size distribution; the sensitivity limit is pushed to smaller diameter objects, potentially allowing for observations to span a break in the size distribution. In fact, we believe that this is exactly what we have observed in our scattering sample, which enables our conclusions.

Trujillo et al. (2000) reported the first, and prior to this work the only, estimate of the scattering object size distribution. With their three detections, and using a previous detection from a different survey, they found that the size distribution was equally consistent with $\alpha = 0.4$ and $\alpha = 0.6$. This small sample result is not a robust determination of the slope and is mentioned only for completeness.

See Section 2.3.1 for plots and further discussion of the scattering process.

1.3.3 Neptune Trojans

Trojans are planetary bodies that roughly share a planet's orbit and remain near the L4 (60° ahead of the planet) or L5 (60° behind) Lagrange points. There are seven confirmed Neptune Trojans (see Table 4.1). The Neptune Trojans have a "hot" inclination distribution, which must have been "frozen-in" to the Trojan's source population prior their capture (Sheppard and Trujillo, 2006).

The deep Magellan 6.5 m survey by Sheppard and Trujillo (2010) had the surprising result of zero detections for intermediate-sized Trojans in the faintest two magnitudes of the survey. Combining all of the Trojans, Sheppard and Trujillo (2010) found that a slope of $\alpha = 0.8$ is consistent with the Trojans larger than a sudden observed paucity of intermediate sized Trojans (starting around $D < 70 - 100$ km). Their non-detection of intermediate-sized Trojans means that the steep power law of $\alpha = 0.8$ cannot continue. Although we believe there are flaws in the analysis in Sheppard and Trujillo (2010) (highly selective binning, use of two objects which are not identified nor confirmed as Trojans, no binning across surveys), the non-detection of intermediate-sized Trojans is robust and necessitates a break in the size distribution. See Section 4.6.2 for a detailed look at the Trojan size distribution and a unified explanation for the lack of intermediate-sized Trojans.

1.3.4 Jupiter Family Comets

The comets which are dynamically controlled by Jupiter are known as the Jupiter Family Comets. The JFCs all lie near Jupiter, with pericentres inside Saturn (Fig. 1.5). Because of Jupiter's strong gravitational influences, close encounters have a high probability of unbinding orbits, and thus JFCs have short lifetimes (10^5 yrs, significantly less than the age of the Solar System). Given that JFCs currently exist, there must be a resupply mechanism for them. The hypothesis that leakage from the stable Kuiper Belt (Duncan et al., 1987; Edgeworth, 1943; Fernandez, 1980) could be the source has since been shown to not work (Levison and Duncan, 1997). Duncan and Levison (1997) proposed that JFCs are instead being supplied by the scattering objects. Volk and Malhotra (2008) examined the feasibility of scatterers as the source, the main question being "are there enough scatterers to supply the JFCs?" Because all observed JFCs are small (km scale, $H \simeq 18$), Volk and Malhotra (2008) used the size distribution from Bernstein et al. (2004), the deepest Kuiper Belt survey to date. The Bernstein et al. (2004) analysis modelled the slope as rolling over to a negative slope at $D \sim 100$ km ($H_g \simeq 9$), the continuation of which forces the conclusion that there are not enough scattering objects to supply the JFCs (Volk and Malhotra, 2008). This problem is addressed by our work.

The JFCs are another "hot" population, with an extended i distribution (See Fig. 1.4). Measurements for the slope of the JFCs find a slope of about $\alpha = 0.5$ (Solontoi et al., 2012; Tancredi et al., 2006), which is approximately the collisional equilibrium slope (n = 3.5). All observed JFCs are small, and so it is reasonable to expect that they are the product of collisional grinding. The JFCs require a source, and must be drawn from the small size, collisionally evolved tail of this source population.

1.4 Research Goals

Size distributions are key diagnostics for the accretional processes and collisional evolution of small-body populations. Measurements of the size distributions for the TNO populations has found that there is a difference between the "hot" and "cold" populations, and that there must be a break in the size distribution. We present a measurement of the scattering objects' size distribution and find a divot distribution. Using this measurement, we present a scenario in which all hot populations in the outer Solar System share a common source. This links the scattering objects with the JFCs (as a source) and the Neptune Trojans, and simultaneously explains mysteries

for these "hot" populations.

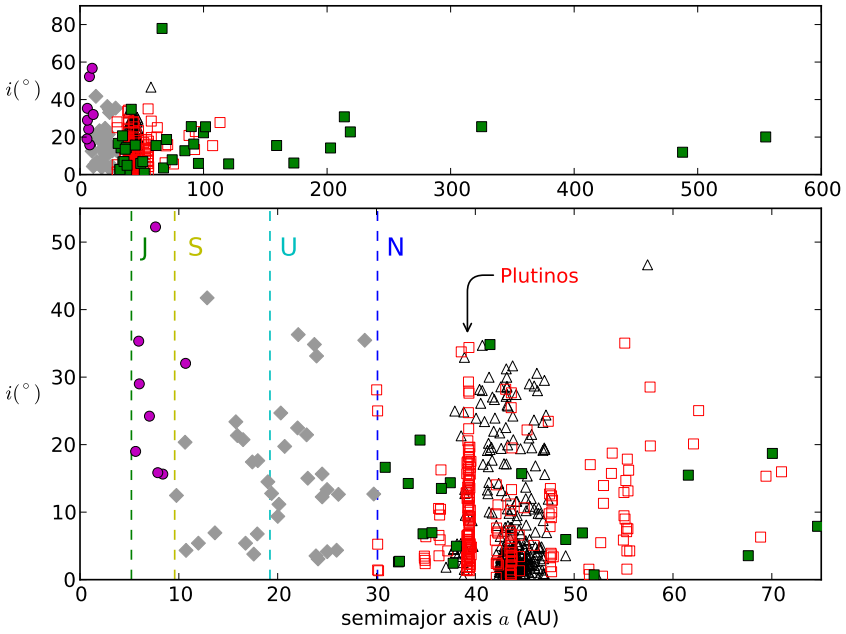

Figure 1.4: A plot of i vs a for detected outer Solar System objects. The upper panel spans all detected a values, while the lower panel provides a zoom to better view the structure around the Kuiper Belt. Many outer Solar System populations are shown: main Kuiper Belt (black open triangles), resonant objects (red open squares), Jupiter Family Comets (purple circles), Centaurs (gray diamonds), and scattering objects (green squares). Dashed lines indicate the locations of the giant planets. This plot is a compilation of the orbits held in the public database from the International Astronomical Union's Minor Planet Center.

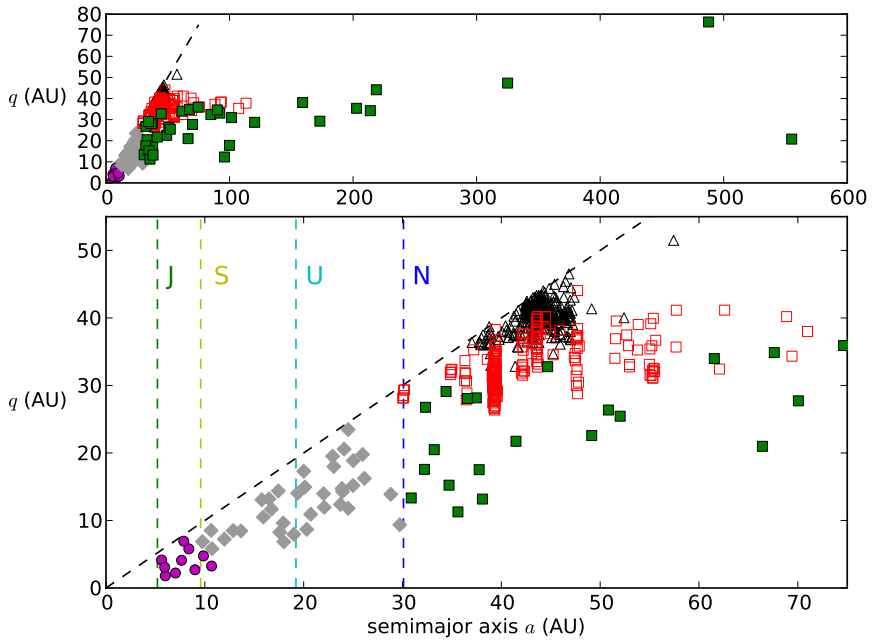

Figure 1.5: A plot of q vs a for detected outer Solar System objects. The upper panel spans all a values, while the lower panel provides a zoom-in. Symbols and colours are as in Figure 1.4. The dashed black line denotes circular obits.

Chapter 2

Measuring the Size Distribution

To measure a size distribution, an observational survey, its detection biases, and a model are needed. The tremendous biases inherent in a survey, often compounded by the small number of detections, prohibit a direct measurement of the size distribution from the observations alone. An orbital model, subjected to the survey's biases, is compared with the detections to constrain the form of the size distribution. This chapter covers the Canada France Ecliptic Plane Survey, its survey simulator, the orbital models used, and how they all tie together to measure the size distribution.

2.1 CFEPS and its Survey Simulator

The Canada France Ecliptic Plane Survey was designed to produce a catalogue of TNOs, while accurately documenting the survey's biases. Precisely knowing the biases allows for a quantitative comparison of theoretical models and observations via the CFEPS survey simulator. As its name suggests, CFEPS surveyed the ecliptic, covering $\sim 320\text{deg}^2$ and seeing to depths in g-band in the range 23.5–24.4 magnitude. A catalogue of 169 TNOs with precise orbits, including 9 scatterers (Table 2.1) was reported. A follow-up survey looking at higher latitudes, carried out in a similar fashion, found two scatterers (HL8a1 and HL7j2) that are included in this analysis; henceforth CFEPS refers to the Canada France Ecliptic Plane Survey and its extensions.

The survey simulator determines the observability of a test object. Given an orbit, the simulator assigns the object an absolute magnitude, places it on the sky and then checks all of the CFEPS blocks for the object, applying all of the observational biases (magnitude limit, survey rate cuts, detection efficiency) to determine if CFEPS would have detected the object. The simulator models all of the CFEPS observational blocks, with their particular magnitude limits and detection efficiencies. The magnitude limits and de-

tection efficiencies were determined by implanting artificial objects into the survey, and then running them through the detection pipeline. For more on the calibration of CFEPS see Petit et al. (2011). With an orbital element model and a size distribution as inputs, the simulator builds a set of absolutely calibrated simulated detections which can then be compared with the observed CFEPS sample.

Designation	**a (AU)**	**e**	**i (deg)**	**d (AU)**	$\mathbf{H}_g$
L4k09	30.19	0.18517	13.586	26.63	9.5
HL8a1	32.38	0.37406	42.827	44.52	7.3
L4m01	33.48	0.33308	8.205	31.36	8.9
L4p07	39.95	0.28088	23.545	29.59	7.7
L3q01	50.99	0.484	6.922	38.17	8.1
L7a03	59.61	0.43949	4.575	46.99	7.1
L4v11	60.04	0.62928	11.972	26.76	10.0
L4v04	64.10	0.50638	13.642	31.85	9.1
L4v15	68.68	0.6999	14.033	22.95	9.0
HL7j2	133.25	0.72374	34.195	37.38	8.4
L3h08	159.6	0.7613	15.499	38.45	8.0

Table 2.1: The CFEPS actively scattering sample (Petit et al., 2011), with two additions from the unpublished High Latitude follow-up survey, HL8a1 and HL7j2, provided by Brett Gladman. All digits are significant.

The survey simulator was provided by Jean-Marc Petit, and modified by the author to accommodate "knee" and divot size distributions, the specifics of the models used, and for easy deployment on a computing cluster.

2.2 Drawing H-magnitude Distributions

A single power-law has a well known and integrable form. As with all integrable functions, it is a simple matter to generate random numbers from this distribution. Divot and "knee" distributions are simply composed of two single power-laws, either joined at a "knee", or with a disconnect. To draw from such a distribution, one simply needs to know the number in one segment of the distribution as a fraction of the whole distribution, and then draw from each segment by their appropriate fraction. This section derives the relative fractions for a divot case, and the "knee" case is found by setting the divot contrast c to 1.

As shown in Fig. 1.1, a divot is defined by a bright slope α_b, a divot magnitude H_d, a divot contrast c and a faint slope α_f. The divot contrast is the ratio of the number of objects in an infinitesimal bin before the divot, to the number in an infinitesimal bin after the divot. If c=1, then the distributions meet and it is a "knee". To find the relative fractions, the normalisation constant, k, must also be considered, though it does not appear in the final equation for the fraction of objects before the divot.

The number of objects in an infinitesimal H-magnitude range is given by

$$\frac{\mathrm{d}N}{\mathrm{d}H} = k\,\alpha\,\ln(10)\,10^{\,\alpha H} \tag{2.1}$$

The number of objects in an H range at $H = H_d$ is given by N_d

$$\frac{\mathrm{d}N}{\mathrm{d}H} = k_b\,\alpha_b\,\ln(10)\,10^{\,\alpha_b H_d} = N_d \tag{2.2}$$

The bright and faint distributions are then matched at the divot, according to the divot contrast, with c being the ratio of the differential number before to after the divot:

$$\frac{\mathrm{d}N}{\mathrm{d}H} = k_f\,\alpha_f\,\ln(10)\,10^{\,\alpha_f H_d} = \frac{N_d}{c} \tag{2.3}$$

Equating Equation 2.2 and Equation 2.3 to solve for k_f gives:

$$k_f = k_b\,\frac{\alpha_b}{\alpha_f}\,\frac{10^{\,\alpha_b H_d}}{10^{\,\alpha_f H_d}\,c} \tag{2.4}$$

To find the cumulative number of objects before the divot, N_{bd}, integrate Equation 2.1 from $-\infty$ to H_d

$$N_{bd} = \int_{-\infty}^{H_d} \mathrm{d}N = \int_{-\infty}^{H_d} k_b\,\alpha_b\,\ln(10)\,10^{\,\alpha_b H}\mathrm{d}H = k_b\,10^{\,\alpha_b H}\,\Big|_{-\infty}^{H_d} \tag{2.5}$$

$$N_{bd} = k_b 10^{\,\alpha_b H_d} \tag{2.6}$$

To find the cumulative number after the divot, N_{ad}, integrate Equation 2.1 from H_d to an arbitrary faint cutoff H_f

$$N_{ad} = \int_{H_d}^{H_f} k_f\,\alpha_f\,\ln(10)\,10^{\,\alpha_f H}\mathrm{d}H = k_f\left(10^{\,\alpha_f H_f} - 10^{\,\alpha_f H_d}\right) \tag{2.7}$$

Inserting Equation 2.4 in to Equation 2.7 gives

$$N_{ad} = k_b \frac{\alpha_b}{\alpha_f} \frac{1}{c} 10^{\alpha_b H_d} 10^{-\alpha_f H_d} \left(10^{\alpha_f H_f} - 10^{\alpha_f H_d}\right) \tag{2.8}$$

Simplifying Equation 2.8 and inserting Equation 2.6 gives

$$N_{ad} = N_{bd} \frac{\alpha_b}{\alpha_f} \frac{1}{c} \left(10^{\alpha_f (H_f - H_k)} - 1\right) \tag{2.9}$$

The important quantity required to generate an H-magnitude distribution with a "knee" or divot is the ratio $\frac{N_{bd}}{N_{tot}}$ where $N_{tot} = N_{bd} + N_{ad}$

$$N_{tot} = N_{bd} \left(1 + \frac{\alpha_b}{\alpha_f} \frac{1}{c} \left(10^{\alpha_f (H_f - H_d)} - 1\right)\right) \tag{2.10}$$

And finally $\frac{N_{bd}}{N_{tot}}$ is given by

$$\frac{N_{bd}}{N_{tot}} = \left(1 + \frac{\alpha_b}{\alpha_f} \frac{1}{c} \left(10^{\alpha_f (H_f - H_d)} - 1\right)\right)^{-1} \tag{2.11}$$

Note that the fraction depends only on the two slopes, the H-magnitudes of the divot and faint end, and the contrast. Equation 2.11 gives the fraction of objects in the bright distribution. To draw from a divot distribution, one simply draws from the two different single power-laws, over the appropriate H ranges, drawing from each such that they contain the appropriate fraction of objects. Section A provides sample code for drawing from a divot or "knee" distribution.

2.2.1 Divergent Mass for $\alpha > 0.6$

It is simple to show that the total mass diverges if $\alpha > 0.6$ (which corresponds to $q > 4$).

The mass in a given range is

$$\mathrm{d}M = \mathrm{d}N(D) \cdot M(D) \tag{2.12}$$

Using Equation 1.1, the total mass is then given by

$$M_{tot} \propto \int_{D_{min}}^{D_{max}} D^{-\mathrm{n}} \frac{4}{3} \pi D^3 \rho \, \mathrm{d}D \tag{2.13}$$

$$M_{tot} \propto \frac{1}{4 - \mathrm{n}} \left(D_{max}^{4-\mathrm{n}} - D_{min}^{4-\mathrm{n}}\right) \tag{2.14}$$

For n > 4 ($\alpha > 0.6$), the exponents are negative and as $D_{min} \to 0$ Equation 2.14 diverges to ∞. So clearly the $\alpha > 0.6$ distributions must become shallower at some H_g magnitude.

2.3 Numerical Models of the Orbital Distribution

The survey simulator does not directly allow for the constraint of a size distribution, but instead, the "testable" quantity is the joint proposal for the orbital distribution and the size distribution. One thus needs an externally supplied orbital distribution for the scattering population. Two such models for the current orbital distribution of large-a TNOs were combined with candidate size distributions and compare to the observed CFEPS sample. Scattering objects were extracted from each model using the criteria explained in Section 1.3.2.

2.3.1 KRQ11

When the giant planets accreted to their present masses (a quick, run-away gas accretion process), they quickly scattered out the nearby planetesimals. Many planetesimals were unbound from the Solar System, many other were scattered out to form the Oort Cloud (with some help from the galactic tides and passing stars), and some found stable regions between 30 and 1000 AU to occupy for the age of the Solar System. The scattered objects retain a close pericentre (as they are in bound orbits, they must return to where they started). This results in a distribution of objects with similar pericentres and widely ranging semimajor axes. If they are scattered far out enough, the tides begin to pull at them at apocentre (when they have virtually no velocity relative to the Sun), and these small pulls circularise orbits by lifting the pericentres. For a more in depth review of scattering in the early Solar System see the review by Gladman (2005).

Two modified versions of Kaib et al. (2011b) (henceforth KRQ11), one initially dynamically "cold", the other "hot", were used. KRQ11 models the gravitational effects of the giant planets, passing stars and the galactic tides on a disk of "massless" planetesimals over the age of the Solar System. The end-states of the modified KRQ11 simulations were provided by Nathan Kaib, with iterative input from Brett Gladman and the author. While KRQ11 examines the effects of different solar environments on the structure of the Oort Cloud, we use the control simulations from KRQ11 as they assume a local galactic environment like our current one.

KRQ11 has an initial disk of planetesimals placed between a=4 AU and a = 40 AU with the surface density proportional to $a^{-3/2}$. The initially "cold" simulation implants test particles with eccentricities, e, less than 0.01 and $i < 1.5°$. The four giant planets are emplaced on their present day orbits, and this system is integrated forward for 4.5 Gyrs. The effects on the evolving particles due to galactic tides and passing stars are also modelled. For further details on the model's specifics see Kaib et al. (2011a) and Kaib et al. (2011b).

It became apparent that no matter which size distribution was used, a match to the present inclination distribution could not be found; the inclinations were too "cold". The scattering out of planetesimals does not vertically "heat" the initially "cold" inclinations enough to match the observations - a previously known problem (Petit et al., 2011). We then asked for a new initially "hot" model, which was provided by Nathan Kaib. The "hot" model draws initial inclinations from the distribution $N(i)\mathrm{d}i \propto \sin i\, e^{(-i/(2\sigma^2))}$, with $\sigma = 12°$, and is identical to the "cold" model in all other ways. See Section 4.1 for further details on the necessity and effects of the "hot" distribution.

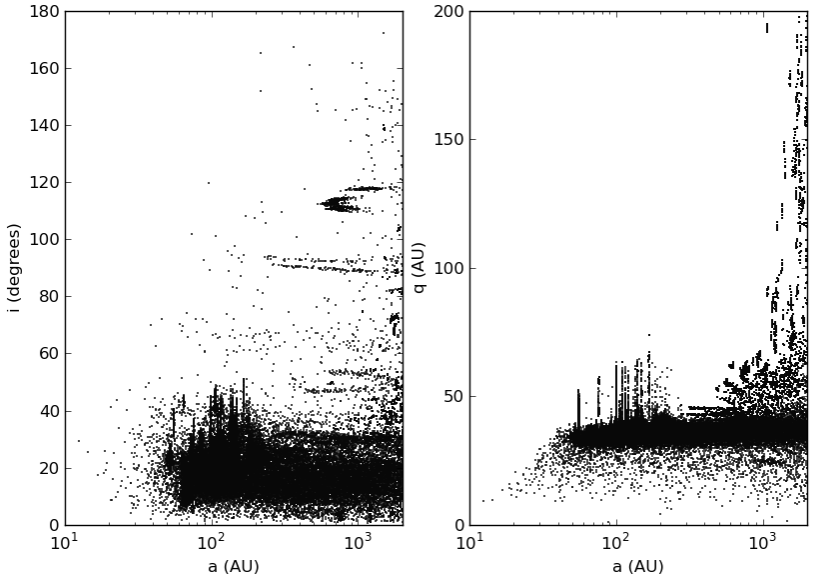

Figure 2.1: The end-state of the modified KRQ11 "hot" model for $a <$ 10 000 AU. See text for discussion.

Figure 2.1 shows the full end state for the "hot" KRQ11. The test particles, which all started within 40 AU, are scattered out to over thousands of AU by the giant planets across the lifetime of the Solar System. The right panel of Fig. 2.1 shows a band of objects scattered out with pericentres $q = 30 - 40$ AU. Also visible in this panel are resonant "fingers" at some semimajor axes, where scattering objects have been trapped in mean-motion resonance with Neptune. On the far right of this panel, test particles are starting to have their pericentres lifted by the galactic tides; this is the inner edge of the Oort Cloud. The left panel of Fig. 2.1 shows some high inclination objects, which are returning from the Oort Cloud with inclinations raised by galactic tides. All of these test particles have been scattered out by the giant planets (dominantly) or passing stars, but many of them have found meta-stable states where they are not strongly affected on short timescales. Today's actively scattering population is likely just the temporal vestigial tail of the TNOs which were scattered out, and formed these meta-stable populations and the Oort Cloud.

Figure 2.2 shows only the scattering objects from the "hot" KRQ11, selected via the criteria in Gladman et al. (2008). Note that the resonance "fingers" have been removed, as well as some large pericentre objects, as they are not scattering. Figure 2.3 shows in more detail the distributions for the subset with $a < 1000$ AU, as CFEPS was not strongly sensitive to those beyond $a = 1000$ AU. Note that the a and i distributions are relatively flat, and that most objects have q between 30 and 40 AU. There are a few retrograde objects ($i > 90°$ which orbit "backwards"), but they are a negligible fraction (see Fig. 2.3).

2.3.2 Gladman and Chan '06

To test the sensitivity of our result to the model's initial conditions we also use the Gladman and Chan (2006) model, which includes an additional two Earth-mass rogue planet (ejected after about 200 Myr), does not have planet migration, and does not model the effects of passing starts nor the galactic tides. The Gladman and Chan (2006) model features and the sensitivity of our result to the selection of a model are discussed in Section 4.5.

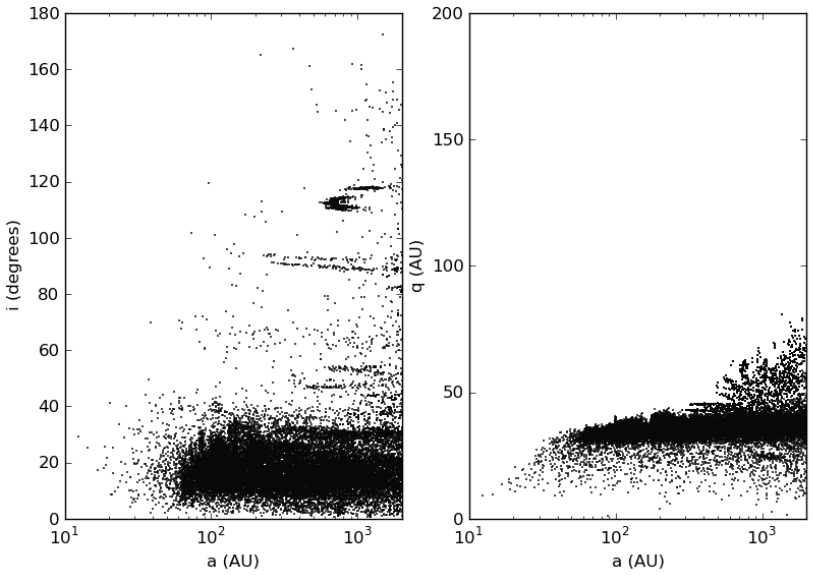

Figure 2.2: The end-state of the modified KRQ11 "hot" model for $a < 10,000$ AU, showing only the actively scattering objects. Beyond $a \simeq 100$ AU the $q < 40$ AU limit on scattering objects begins to raise because more weakly-bound orbits more easily feel the scattering effects of the giant planets while interior to 100 AU heliocentric distance.

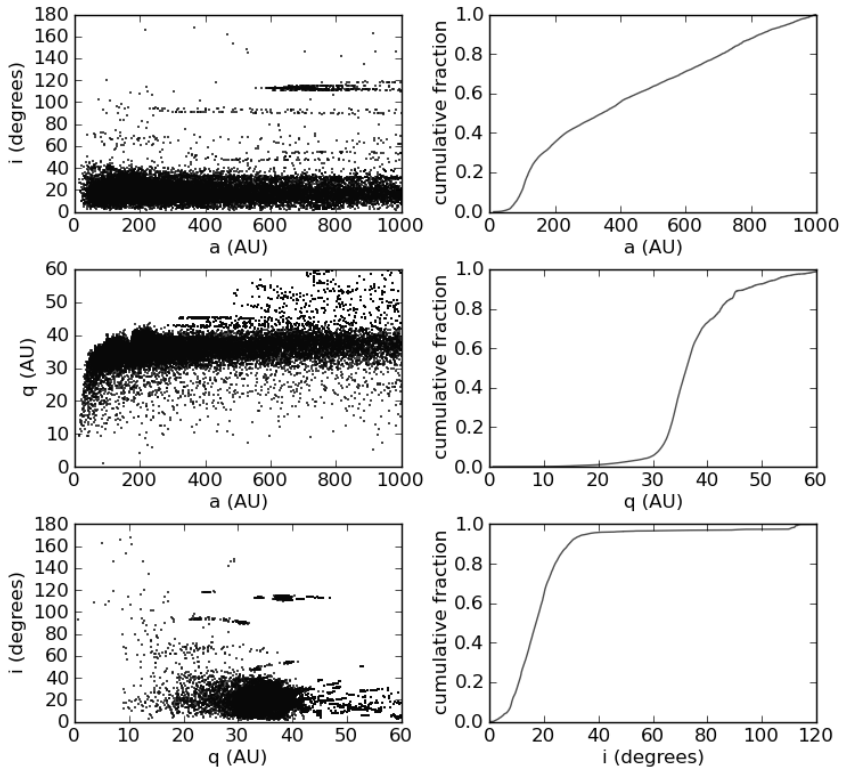

Figure 2.3: The orbital parameter distributions for the actively scattering objects from the "hot" KRQ11 model. The three left panels show greater details of the scattering object initial distribution for $a < 1000$ AU. Objects with $a > 1000$ AU have negligible detection probability. The right column shows the cumulative distributions for a, q and i.

Chapter 3

Methods

This chapter covers the details of combining the orbital models with a candidate size distribution for comparison with the CFEPS scattering sample. This work uses the modified version of KRQ11 as its main model, and so this chapter is discussed in the context of KRQ11 (the same process used for both the initially "hot" and "cold" versions). This methodology was also carried out for the Gladman and Chan (2006) model, which was used to test the sensitivity of our result to the model's particular parameters.

3.1 Implementation of the Survey Simulator

The scattering objects extracted from KRQ11 constitute the model of the present day orbital distribution, which is then passed to the CFEPS survey simulator. Objects are drawn at random from the model sample, with their specific a, i, q values. Because there can be no resonant scattering objects, the precise values of an objects orbital parameters should not be special, thus the object is placed at a random point on its orbit and the orbit randomly oriented, with the argument of pericentre, argument of periapsis and mean anomaly all chosen randomly. To smooth the orbital distributions of the finite model, the a, q, and i values are randomly perturbed; a and q by $\pm 10\%$, and i by $\pm 1^\circ$. Each object is then assigned an H_g from a candidate distribution and its observability is assessed. The end result is a set of simulated detections which have known a, q, i, H_g, and distance at detection d values. These five parameters are used to assess the quality of a match.

3.2 Comparison and Statistics

Taking the input orbital model as correct (see Section 4.5 for justification), we test each candidate H_g distribution by comparing the five parameters a, q, i, H_g, and d of the simulated detections to the CFEPS sample. The Anderson-Darling (AD) statistic (Kavelaars et al., 2008) is used to quantify the comparison. The AD statistic is a 1-D distribution test similar to the

Kolmogorov-Smirnoff test, but more sensitive to differences in the distribution's tails. The AD statistic tests if a distribution (the CFEPS sample) can be drawn from a source distribution (the simulated detections). As there are 11 real CFEPS scattering objects, a random set of 11 objects is drawn from the simulated detections and its AD distance from the CFEPS sample calculated. This process is booststrapped, providing a final AD statistic distribution, which allows one to determine the fraction of the bootstrapped samples where the CFEPS sample can be said to have been drawn from the simulated detections. An AD statistic of 5% rejects the hypothesis that the CFEPS distribution is drawn from the simulated detections at the 95% level; this is a rejection of the candidate H_g size distribution used to generate the simulated detections. Figure 3.1 shows the simulated detections (blue) of a candidate H_g distribution (a single power-law) and the CFEPS sample (red), with the AD statistics; this candidate distribution is rejectable at the 99% level for the H_g distribution.

Although iterative tuning of the H_g distribution occupied much of our efforts, one result became evident early. For the initially "cold" KRQ11 it was found that the i distributions were too cold (see Fig. 3.2 Section 4.1). This work uses the initially "hot" KRQ11 generated to nicely resolve this problem, which drastically improves the i distribution matches, indicating that the planetesimals scattered out of the zone of the giant planets already had significant orbital inclination before scattering started. There is, however a trade off between the agreement of the i and a distributions. The "hotter" model improves the i, while weakening the a distribution. We believe that this simply points to a question of how "hot" the initial disk needed to be, and that an intermediate initial inclination width will allow for both the i and a distributions to match well (see Section 4.7). This work's constraints on the scattering population's size distribution come solely from the "hot" KRQ11 model.

For each candidate size distribution coupled with the "hot" KRQ11, we assess the AD statistic for q, i, H_g, and d, and determine an acceptability level for the size distribution from the AD statistic which is most rejectable. If any of these AD statistics is rejectable, we then reject the candidate H_g size distributions. Because of the noted problem with the a distribution, we do not include the AD statistic for a in this analysis, though its inclusion does not alter our conclusion. Figure 3.2 shows, as an example, the cumulative distributions for the "cold" single power-law candidate size distribution. The three lower panes are all rejectable at the 99% level, and so this candidate size distribution is rejected.

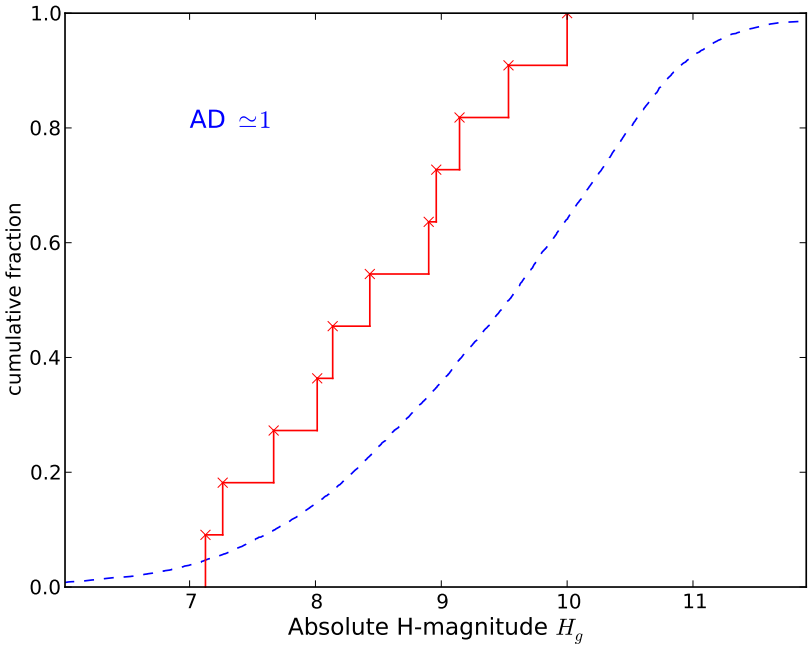

Figure 3.1: An example of a model rejected using a 1-D distribution. The blue dashed curve is the observationally biased H_g distribution for the "cold" KRQ11 model from a single power-law with $\alpha = 0.8$. The red distribution is the real CFEPS observations' H_g distribution. AD $\simeq 1$ means that only 1% of the bootstrapped 11-object samples drawn from the dashed blue simulated detections showed a larger variation than the true sample; this is thus a 99% rejection of the dashed blue distribution.

3.3 Size Distributions Used

As discussed in Section 1.2 this work considers three kinds of size distributions: single power-law, "knee", and divot. The single power-law case only has one parameter: the slope α. The divot case has four parameters: the bright side slope α_b, the faint side slope α_f, the H magnitude of the divot, and the divot contrast c as shown in Figure 1.1. "Knees" are a special case of divot with $c = 1$, and a single power-law is a special case of divot where $c = 1$ and $\alpha_b = \alpha_f$.

The "hot" TNO populations have a measured slope of $\alpha = 0.8$, although

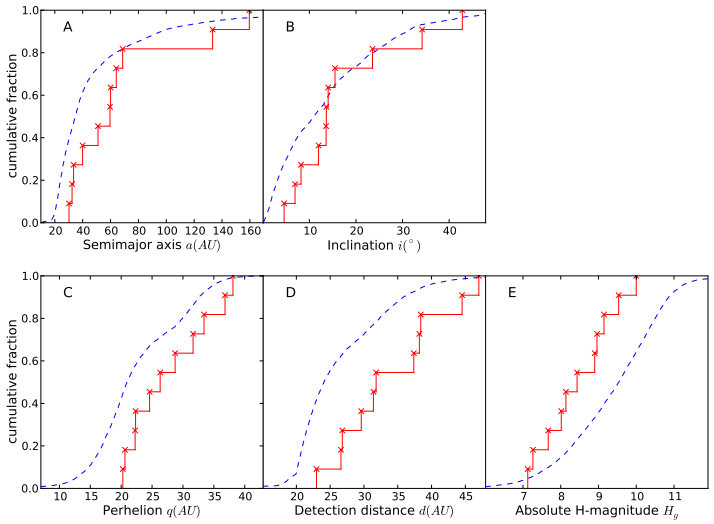

Figure 3.2: A sample set of distributions for a, q, i, H_g, and d. The blue dashed curves are the simulated detections for the "cold" KRQ11 model from a single power-law with $\alpha = 0.8$. The red distribution is the real CFEPS observations' H_g distribution. This candidate size distribution fails because the three distributions on the bottom row are all rejectable at the 99% level, but this can be resolved with a different size distribution.

there is evidence that this steep slope must break at smaller sizes (see Chapters 1 and 2); we thus fix the bright end (large size) slope α_b to 0.8. Recent measurements of the "hot" Plutinos (Gladman et al., 2012) and the "hot" Classical belt (Petit et al., 2011) show that a single power-law fits the hot populations down to the survey sensitivity limits H_g of 9 and 8 respectively. Our observations require a break in the size distribution. If we restrict our sample to $H_g < 9$, a single power law fits our observations. We require a break in our observations' range and so we fix our knee/divot break at $H_g = 9$ ($D \simeq 100$ km). This leaves the faint slope α_f and the contrast c as the only free parameters.

3.4 Grid Search

A grid of c and α_f pairs was explored. Values for α_f ranged from -0.5 to 1.2 in steps of 0.1, encompassing the most negative faint (Bernstein et al., 2004) and steepest (Petit et al., 2011) slopes proposed for the "hot" population. Values for the contrast ranged from 10^0 to 10^3 in logarithmic steps of 0.25. For each run of the survey simulator the candidate size distribution was coupled with the scattering set from the initially "hot" KRQ11 model. Ten thousand simulated detections were found for each case, in order to produce a well sampled simulated detection distribution. For each grid point the AD statistic was calculated for the q, i, H_g, and d distributions, with the most rejectable of these being recorded. Candidate size distributions are assessed on their most rejectable AD statistic. The computed AD statistics allow us to generate confidence regions for the two free parameters (c, α_f).

Chapter 4

Results and Extensions

4.1 Inclination Distribution

Results later in this section imply that the perihelion and semimjaor axis distributions retain little memory of their initial conditions because they are the result of a 4 Gyr random walk process (Duncan et al., 1987). In contrast, the current orbital inclination distribution for the scattering objects is influenced by (a) the process of scattering with Neptune (which does not efficiently transform the in-plane speeds to out-of-plane speeds), and (b) the initial inclination distribution of the planetesimals when they giant planets formed and began scattering them outwards. The current inclination distribution thus does contain some memory of the state of the planetesimal disk ~ 4 Gyr ago.

Candidate size distributions were initially tested with the "cold" model, but it was found that all size distributions were rejectable at the 95% level. Rejectable meaning that the most rejectable of the AD statistics for a, i, q, d, and H parameters was rejectable at the 95% level. For the majority of cases, it was the inclination distribution which failed most; clearly the inclinations were too "cold". A "hotter" KRQ11 model was then computed by Nathan Kaib, with input from Brett Gladman and the author. This "hotter" initial model addressed the inclination problem. Figure 4.1 shows a comparison of the initially "hot" and "cold" inclination distributions for the same candidate size distribution. The initially "cold" simulated detection distribution has 50% of the inclinations below $\sim 8°$, whereas the CFEPS observations have 50% below $\sim 13°$; too many of the "cold" model objects have low inclinations and so the distribution is rejectable at greater than 99%. With the "hot" model, the inclination distribution matches very well, and the inclination is almost never the most rejectable of the tested parameters. While the "hot" version dramatically improves the i match, it also worsens the a match, though not significantly. There is room for tuning the width of the initial i distribution to better match the a distribution (see Section 4.7).

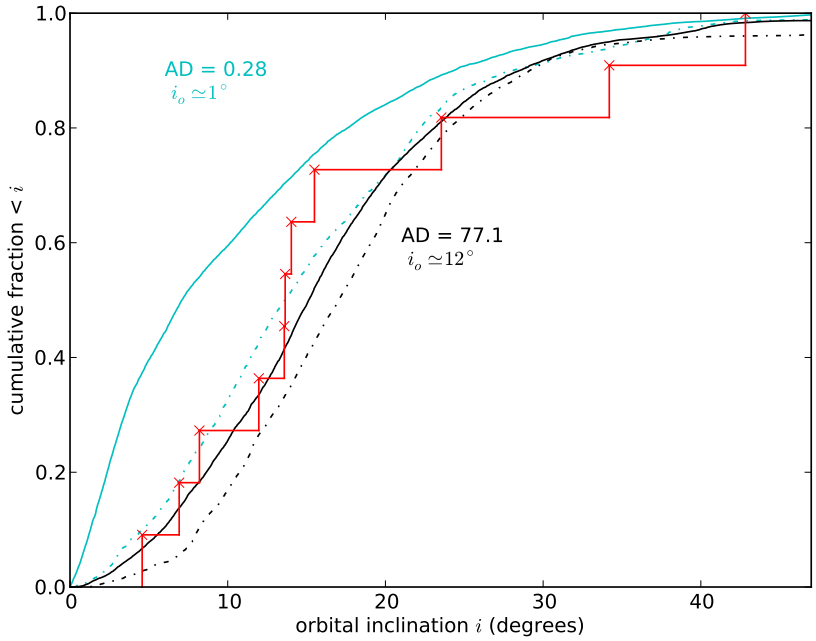

Figure 4.1: The cumulative simulated detection i distributions for the initially "cold" (solid teal) and "hot" (solid black) KRQ11 models. Dashed-dot lines are the intrinsic KRQ11 distributions. The initially "cold" distribution is rejectable at greater than the 99% level, whereas the initially "hot" model results in many fewer scattering objects today having $i < 10$, thus providing an excellent match.

4.2 A Single Power-Law Size Distribution?

With many Solar System populations well fit by a single power-law over a few magnitude ranges, it needs to be established that a single power-law does not match the CFEPS scattering objects. Figure 4.2 shows the simulated detections for the single power-law with $\alpha = 0.8$, which is well established for the "hot" populations. Panel **E** shows that the simulated detections expect 50% of the detected objects to have $H_g > 9$, but only ∼20% of the CFEPS sample have $H_g > 9$; a single power-law produces too many small object detections. While not shown, if one cuts the sample to consider only the $H_g < 9$ scattering objects, a single power-law of $\alpha = 0.8$ provides a good match. Panel **D** shows that a single power-law predicts 50%

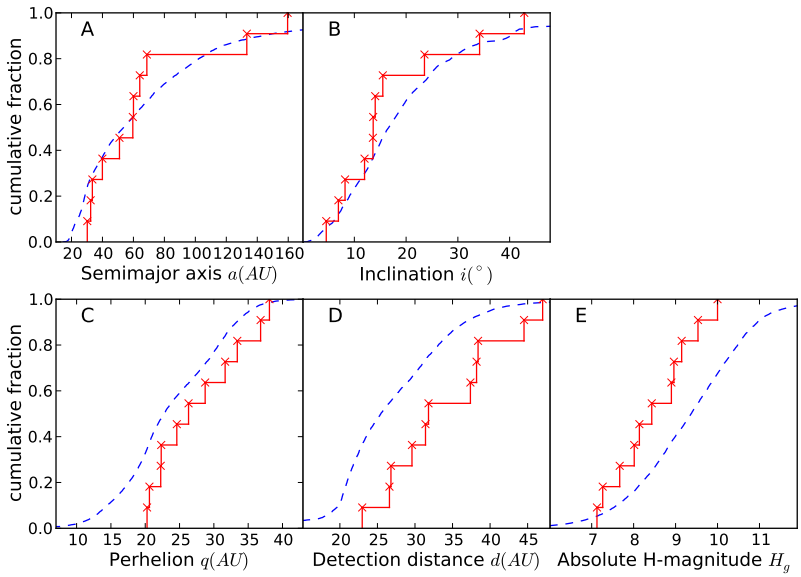

Figure 4.2: The a, i, q, d, and H_g distributions for the single power-law $\alpha = 0.8$ simulated detections (dashed blue) from the "hot" KRQ11. The CFEPS sample is shown in red. The a and i distributions are acceptable, but a single power-law fails on the q, d and H_g distributions.

of objects to be detected inside $d = 25$ AU, but CFEPS only detected one object that close. For an exponential H-mag distribution, the large number of objects just inside the survey's magnitude limit dominate the observed sample. CFEPS did not observe these small objects, despite being sensitive to them as panel **E** shows. A single power-law produces an abundance of small objects, predicted to be detected at close distances; this was not observed. Thus a single power-law was rejected at the 99% level. A break in the size distribution is required to reduce the number of small-sized objects.

4.3 Grid Results and Constraints

Because the literature has often used "knee" distributions where a single power-law fails, considerable time was spent exploring "knee" parameter space. Varying the "knee" location and the slope beyond the "knee" failed to provide a compelling match. We then explored parameterisations which include divots.

To constrain the form of a break in the size distribution, a grid of candidate size distributions (as described in Section 3.4) was tested; the results are shown in Figure 4.3. "Knee" distributions are on the left edge of the plot, with $c = 1$, and a single power-law is marked by the blue star. Divot scenarios provide better matches than "knees" with positive slopes. The CFEPS data set requires a relative lack of small-sized objects. For steeper post-divot slopes a higher contrast value is required to ensure that there is not an abundance of small objects, which were not observed. This creates a band of acceptable (c,α_f) pairings. With this data set we can only rule out a single power-law, and constrain the (α_f,c) pair. Using arguments from other TNO populations in the literature, we identify a preferred model (green star).

Figure 4.3 shows the constraints on the form of the scattering object size distribution. The yellow band denotes cases of equally good matches to the CFEPS data set. "Knees" to negative slopes are acceptable given the CFEPS data set alone (resolved in Section 4.4). Very large ($c \sim 30$) contrasts are allowed if the post-divot slope is large, but this would result in the same mass non-convergence problem if this slope continues. The black dashed line in Fig.ẽfFig:Contours marks the upper bound for slopes which converge. There are many acceptable matches. Further constraints can be found from other outer Solar System populations.

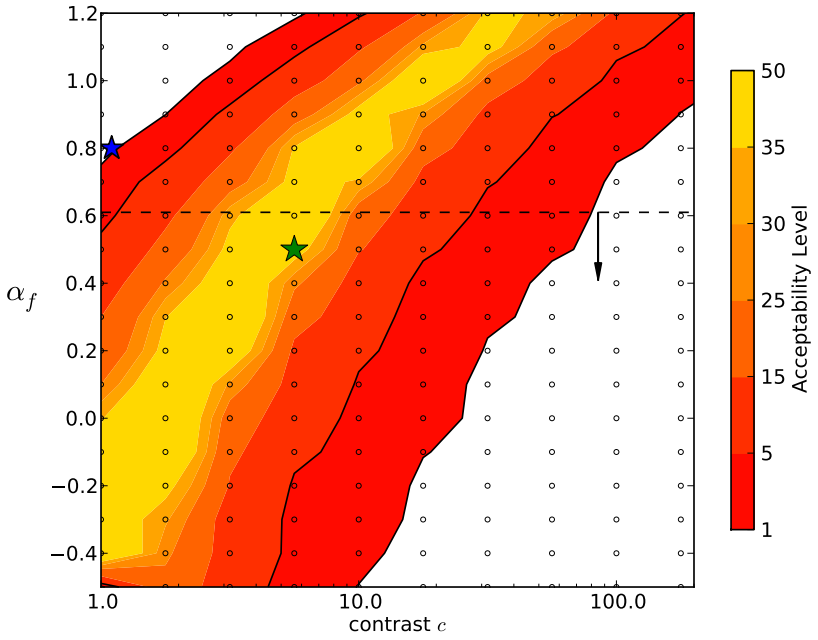

Figure 4.3: A contour plot of the rejectability level for candidate size distributions. All size distributions have a bright slope $\alpha_b = 0.8$ to $H_g = 9$. Size distributions then break to the faint slope α_f shown on the y-axis, with the contrast c shown on the x-axis. The left edge of the plot with $c = 1$ shows "knee" distributions. The blue star marks a single power-law of $\alpha = 0.8$, which is rejectable at greater than 99%. The green star marks our preferred divot case (see Section 4.4). The black dashed line marks $\alpha = 0.6$; α_f must be less than 0.6 or else the total mass diverges. The open circles mark the tested candidate distributions.

4.4 Preferred Model

As discussed, the CFEPS scattering sample requires a lack of small-sized objects. Figure 4.3 shows this visually. The best matching models reduce the number of small-sized ($H_g < 9$) objects through either a divot, or a "knee" to a flat/negative slope. There is a distinct difference between these two cases: positive α_f slopes produce a substantial amount of small-sized objects, whereas negative and flat slopes do not. Many scattered objects, and their companion objects (Centaurs, JFCs) have been observed for $H_g \gg$

9 (Fig. 4.4). Negative slopes, and even divots to shallow slopes, would not produce enough small objects to allow for the observed small-size objects (Volk and Malhotra, 2008).

The JFCs, measured in the range $H_g \simeq 14-17$, give a slope $\alpha_f = 0.5 \pm 0.1$ (Solontoi et al., 2012; Tancredi et al., 2006). As the scattering objects are the most logical source of the JFCs, we choose a divot with $\alpha_f = 0.5$ for our preferred size distribution. A divot is singularly capable of explaining both the paucity beyond the break (which necessitates the break) and the recovery needed to produce enough scattering objects to feed the JFCs. The measured rollover to a negative slope for faint TNOs (Bernstein et al., 2004) is consistent with a divot, as a realistic divot would not drop precipitously, but instead would decrease initially with a negative slope and then recover to its post-divot slope. A recent measurement by Fraser et al. (2010) of faint TNOs found a slope $\alpha = 0.4 \pm 0.15$, consistent with our preferred $\alpha_f = 0.5$. We computed the H_g magnitudes for these objects and found that they span the divot, with the majority beyond $H_g = 9$. Having observations which span the divot would tend to flatten the measured slope, which further supports a choice of $\alpha_f = 0.5$. The preferred divot is consistent with the CFEPS observations, observations of faint TNOs, and can explain the source of the JFCs (see Section 4.6.1).

From Fig 4.3 it can be seen that there are two well matching divots with $\alpha_f = 0.5$. The divot with $c \simeq 6$ provides a slightly better match and so was chosen. This size distribution has $\alpha_b = 0.8$ to a divot at $H_g = 9$, with a contrast of $c \simeq 6$ to a faint slope of $\alpha_f = 0.5$. Figure 4.5 shows the cumulative distributions for our preferred divot (green) and the single power-law (dashed blue). The divot provides a very good match, and is not rejectable on any of the distributions (a, i, q, d, H_g).

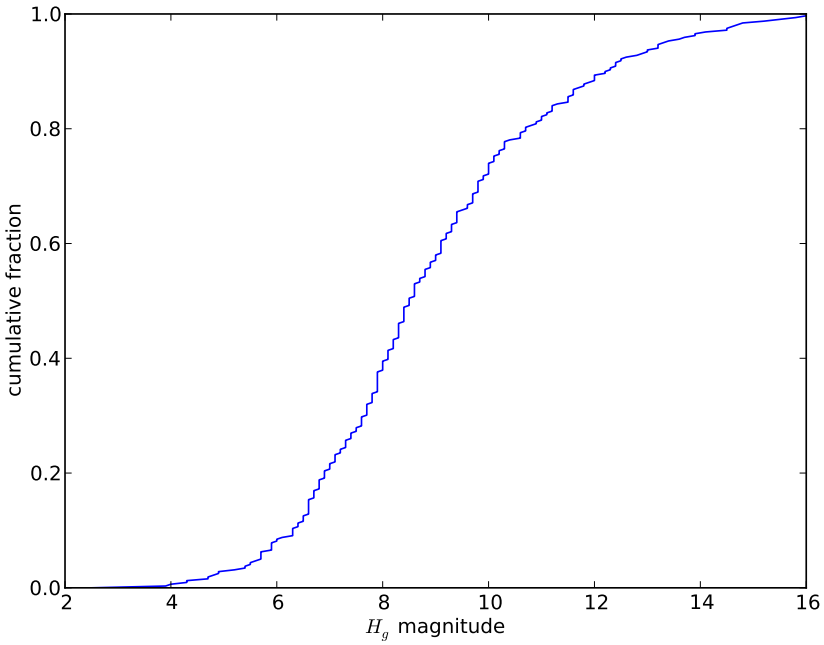

Figure 4.4: A compilation of the scattering objects and Centaurs from the International Astronomical Union's Minor Planet Center (a public database). Complicated selection effects which are combined from many surveys prevent a measurement of the slope or form of the size distribution for this combined sample. The mixing of surveys with different limiting magnitudes means that the termination of the exponential number increase around H_g=8–9 may be due to the surveys' limits starting to prevent detections. Half of the sample has $H_g > 9$, even though only some of the Centaur surveys were sensitive to such small objects; this means that a negative slope past $H_g = 9$ is disfavoured, as very few H_g >12 objects would exist to be detected if the population had an exponentially declining number distribution (negative α).

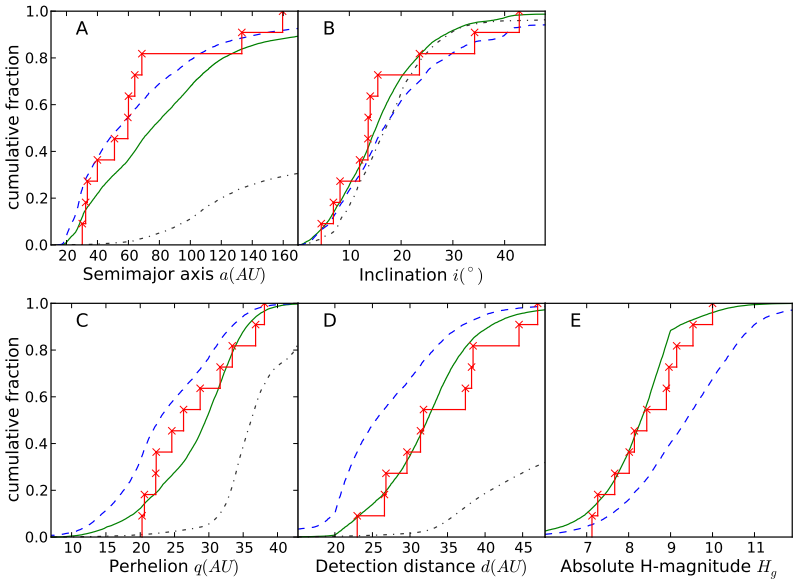

Figure 4.5: Cumulative distributions for a, i, q, d, and H_g. The CFEPS sample is plotted in red, with simulated detections from the "hot" KRQ11 shown in dashed blue for a single power-law and solid green for our preferred divot. The dashed dot distributions in panels **A** - **D** show the intrinsic KRQ11 distributions. The strong observational biases are evident when one compares the intrinsic and the simulated detections distributions.

4.5 Gladman and Chan Model Comparison

Because we do not directly test the size distribution, but instead the joint proposal of the size distribution and orbital model, the effects of the model choice need to be established. KRQ11 produced a model for today's scattering objects, arising from the planets in their current orbits, the effects of the galactic tides, and the effects from passing stars. One might have concerns that the giant planets did not form in their present day locations, as in the Nice model (Gomes et al., 2005; Morbidelli et al., 2005; Tsiganis et al., 2005), or have concerns about the specific parameters for the galactic tides and passing stars used. To examine the sensitivity to the model, we also performed our analysis using the Gladman and Chan (2006) model (GC06). Gladman and Chan (2006) models scattering objects much in the same way as KRQ11. A disc of initially "cold" planetesimals is placed, along with giant planets, and then evolved for the age of the Solar System. GC06 however does not model the effects of galactic tides, planet migration, nor passing stars. GC06 has an additional $2M_{Earth}$ planet in the outer Solar System (ejected at around 200 Myr), which allows us to partially test the sensitivity of our result to the location of the giant planets.

Figure 4.6 shows the cumulative distributions for our preferred divot from both orbital models. GC06 has an initially "cold" disk and so the "cold" KRQ11 model is used for comparison. The results from the two models differ only slightly, and neither is rejectable, aside for their i distributions. This demonstrates that the current distribution of scattering objects is insensitive to the fine details of the dynamical conditions, and that galactic tides and passing stars have a small effect. Today's orbital distribution of scattering objects is dominated by the giant planets. Because GC06 also contains a rogue planet, we conclude that the results are not strongly sensitive to the location of the planets in the outer Solar System. The rejectability of our preferred model is not strongly dependent on the choice of model. We thus constrain the form of the size distribution when the initially "hotter" KRQ11 model, which we believe is the best representation of the evolution of the scattering objects over the 4.5 Gyr Solar System history.

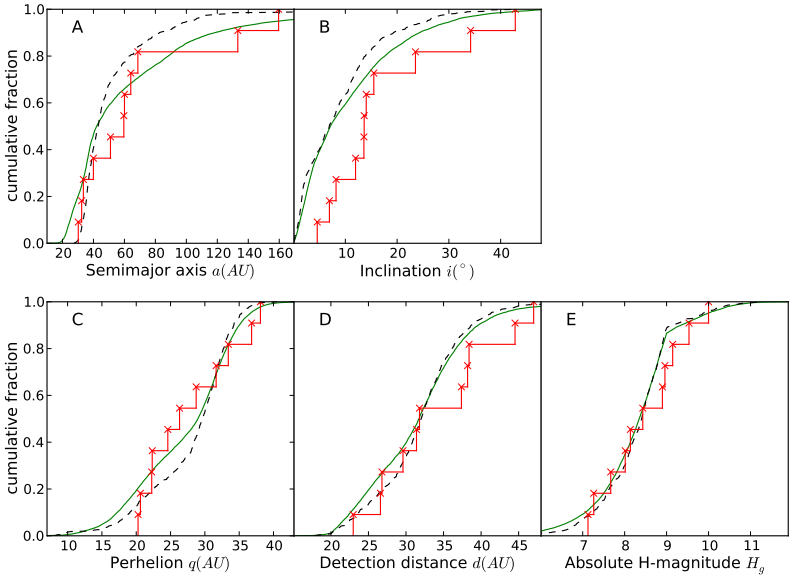

Figure 4.6: Cumulative distributions for a, i, q, d, and H_g. The CFEPS sample (red) is compared with the simulated detections from the Gladman and Chan model (dashed black) and the initially "cold" KRQ11 (green).

4.6 Connections and Interpretations

We favour a scenario in which the "hot" populations all share a common origin. The available constraints imply that a ring of planetesimals with an already heated inclination distribution (of order ten degrees, which is at least an order of magnitude hotter than conditions during accretion would allow) was present in the giant planet region as they arrived at their current masses. In our scenario, a ring of planetesimals with a "heated" inclination distribution formed interior to the current Kuiper Belt. This population would had a divot size distribution, with a slope of $\alpha_b = 0.8$ to around $H_g = 9$ ($D \simeq 100$ km) where it then drops and recovers as $\alpha_f = 0.5$. The slope in the post-divot region was set by mutual collisional evolution, while the steeper slope of 0.8 was set during planetesimal formation. When the giant planets accreted to their present masses, they quickly scattered this population out to a much larger volume. This ended all collisional evolution and thus "froze-in" the size distribution. As this population got scattered

out, parts of it became trapped in mean-motion resonances with Neptune, and as Neptune Trojans in its L4 and L5 points. Many other members were scattered out to form the Oort Cloud, leaving a small tail of scattered planetesimals in the inner Solar System which would constitute the Jupiter Family Comets, the Centaurs, and the scattering objects. We now look to the JFCs and Neptune Trojans to test our preferred size distribution. Note that there are currently no well determined size distribution estimates for the Centaurs.

4.6.1 Population Estimate and JFCs

Measurements for the JFC size distribution come from the abundant, small km scale ($H_g = 19$) comets that come inside Jupiter and are thus easily observed. Since these nearby comets are eliminated by Jupiter on less than Myr time scales, they are re-supplied from the Centaurs (which are eliminated on 10-100 Myr time scales), which are in turn thought to be supplied by the scattering objects (which have enough stability to continue to provide Centaurs even today). Volk and Malhotra (2008) found that at least $2 \cdot 10^8$ scattering objects with $H_g < 19$ are required to supply the JFCs. To test our size distribution, we estimate the size of the scattering population with our preferred divot. The survey simulator is run, requesting 11 (the number of CFEPS observations) simulated detections. Each time the survey simulator tests a model object, this object is counted. The survey simulator draws and perturbs objects from the model until the required 11 simulated detections is achieved. Because CFEPS is absolutely calibrated, the total number of objects drawn for 11 simulated detections gives an estimate of the intrinsic size of the scattering population. This process was bootstrapped, and we estimate that there are $2 \cdot 10^6$ scattering objects with $H_g < 13$, which extrapolates to $2 \cdot 10^9$ scattering objects with $H_g < 19$, providing enough for them to be the JFC source. Figure 4.7 shows our preferred divot with our actual population estimate on the y-axis.

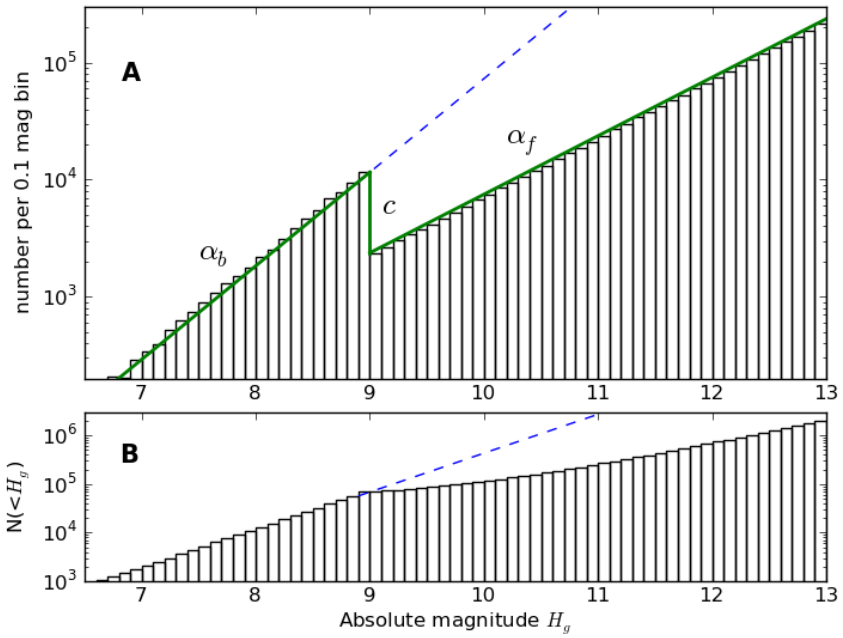

Figure 4.7: Histograms of our preferred divot size distribution. **A**: The differential distribution, with the preferred solution overlayed in green, and an extrapolation of the single-power law with slope $\alpha = 0.8$ beyond H_g shown in dashed blue. The contrast $c \simeq 6$ is the ratio of the bins on either side of the divot. **B**: The cumulative size distribution. The vertical axes show the estimated number of scattering objects with $a < 1000$ AU using the absolute CFEPS calibration.

4.6.2 Neptune Trojans

The Neptune Trojans are a "hot" population, and were captured in Neptune's L4 and L5 points in the scenario where the "hot" populations were transplanted outward in the early Solar System. In this scenario they would have the same size distribution as the scattering objects, and so we apply our preferred divot to the Neptune Trojans.

Because of their low eccentricities, the resonant Neptune Trojans form a set of TNOs which are nearly all at the same distance, making the conversion between apparent and absolute magnitude a single fixed offset of $H_g \simeq g - 14.7$. The dispersed inclination distribution (Sheppard and Trujillo, 2006),

although not yet precisely measured, links these objects to all the other resonant populations, which are also dynamically "hot" (Gladman et al., 2012). Due to their relative proximity at 30 AU, deep observations of the Trojans should reach apparent magnitudes past the break, and the roughly constant distance decreases the confusion caused by detecting objects at a wide range of distance. Sheppard (2010) used detections for Neptune Trojans to argue that beyond $m_R \simeq 23$ (corresponding to $H_g \simeq 9$) there was an absence of Trojans due to non-detection in their survey, and thus smaller Trojans were missing. Under the assumption that the Trojans and other resonant TNOs were implanted from a displaced scattering population and thus share the same size distribution, we confirmed that the size distributions we deduce are not in conflict with the non-detection of small Trojans by these surveys.

The known Neptune Trojans (Table 4.1) are binned and plotted (Fig. 4.8) according to their on-sky surface density; the objects are in half magnitude bins, binned across all surveys simultaneously, with the appropriate weight given to each object. The bins are plotted with 1σ Poisson error bars due to small numbers, which dominate over the small uncertainties in sky coverage. The 2σ upper limits, translated to H_g-magnitude, from Sheppard (2010) are included. Pairings of the contrast and post-divot slope which appear yellow in Fig. 4.3 are plotted. All of the models share a single exponential law with logarithmic slope $\alpha_b = 0.8$ up to $H_g = 9$. Our preferred model (green star in Fig. 4.3, green line elsewhere unless indicated) is coloured in green. This representation is sensitive to bin centres and to the normalization of the slope above the divot (larger objects).

Name	H_g	**Survey**	**Effective Sky coverage**
UP10	9.1	(Sheppard, 2010)	49 deg^2
TN53	9.4	(Sheppard, 2010)	49 deg^2
T074	8.8	(Sheppard, 2010)	49 deg^2
LC18	8.6	(Sheppard, 2010)	49 deg^2
QR322	8.5	(Chiang et al., 2003)	89 deg^2
RJ103	7.8	(Becker et al., 2008)	120 deg^2
Vl305	8.3	(Becker et al., 2008)	120 deg^2

Table 4.1: Neptune Trojans and the effective sky coverage of their respective surveys

Given the uncertainties on the binned data points, and the large degree of flexibility in bin centre choice, there is little additional constraint from

the known Neptune Trojans. Fig. 4.8 and Fig. 4.9 demonstrate the degree to which the choice of bin centres affects the conclusion that there is an observed drop in the differential surface density of Trojans. The strongest constraint comes from the non-detections (Sheppard, 2010), which precludes both a single power-law and a knee to a positive slope.

Given our analysis, the conclusion would not be that small Neptune Trojans are "missing", but rather that the sudden drop results in the population fainter than the divot not recovering in terms of on-sky surface density to at least the value at the divot until $H_g > 11$, by which point the deepest survey lacked the sensitivity to detect them. If this scenario is correct, detection of several small ($H_g > 11$) Trojans would require surveying ~ 100 square degrees of sky to 26th magnitude depth. The $D > 100$ km Trojans could all be found in shallower surveys (and there will only be a few hundred of them), because the divot picks out a "favoured" apparent magnitude for this population which is, unusually, confined to a narrow range of heliocentric distances.

Effectively, the Neptune Trojan data set allows size distributions with very large contrast and strong negative slopes, whereas the scattering object data set requires a steep slope if there is a large contrast, and disfavours negative slopes. The Neptune Trojan set does rule out some large contrast/steep slope scenarios, which our data set would otherwise allow.

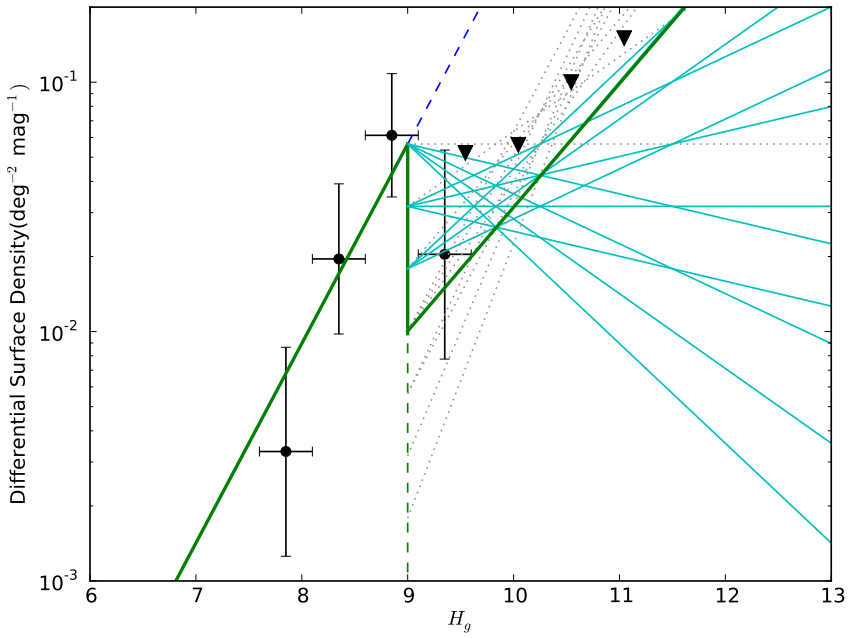

Figure 4.8: The differential luminosity function for the known Neptune Trojans. Vertical error bars are Poisson 1σ limits, horizontal error bars denote bin ranges. Black triangles represent 2σ upper limits as interpreted from Sheppard (2010). The dark blue dashed line is an extrapolation of the single power law. The solid green line is our preferred solution, dotted gray lines are solutions which appear yellow in Fig. 4.3 (thus are not rejectable), and light blue lines are the subset of those which satisfy the 2σ upper limits.

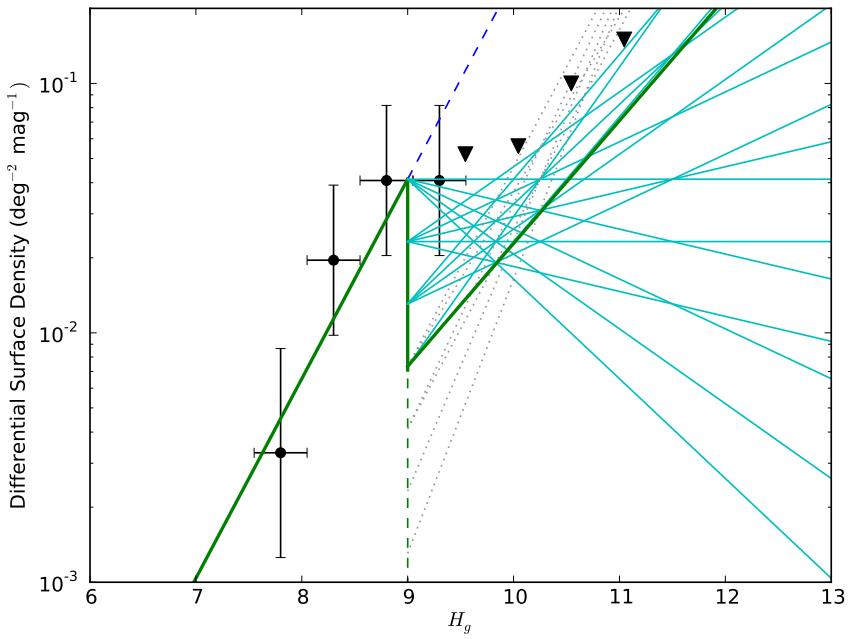

Figure 4.9: A different choice of bin centres for the Trojan data, showing the sensitivity to the choice of visualisation. Line styles and colours are the same as in Fig.4.8.

4.6.3 How Could A Divot Have Formed?

At first appearance, a divot size distribution may seem like an unrealistic and arbitrary construction. There are, however, two scenarios already explored in the literature for producing a divot size distribution. It is possible that the formation physics for small sizes are different, creating a wave in the size distribution. This wave would then propagate upwards in the size distribution with collisional evolution. Smaller objects break up larger ones through collisional grinding. There is a critical size which a smaller impactor must be in order to cause a disruption of a larger object. Larger objects are less frequently destroyed if there is a paucity in their critically sized impactors. Eventually the smaller population builds up from grinding, and the paucity of objects moves to larger size; the wave propagates up the distribution. Fraser (2009) showed that a primordial wave in the size distribution at $D = 2$ km would propagate up to 100 km, leaving a divot in the size distribution.

An alternate theory for forming a divot borrows a new popular idea from the asteroid belt: that objects only form to some minimum size (Morbidelli et al., 2009). The idea here is that planetesimals condense directly into large bodies inside vortices (Johansen et al., 2007) in the protosolar nebula, and smaller bodies only form later from collisional processes. Applying this idea to our preferred divot size distribution gives the following scenario: the "hot" populations accrete into large bodies with a slope $\alpha = 0.8$ down to a size of $\sim$100 km ($H_g \simeq 9$). All smaller objects would form later from collisional grinding. Fortuitously, and completely independently, Campo Bagatin and Benavidez (2012) examined this case amongst many simulations of collisional evolution. They show (their Fig. 6) that an initial distribution with no $D < 100$ km objects evolves into a divot with $\alpha_f \simeq 0.5$ and a contrast of $c \sim 20$ after 500 Myr of collisional evolution. The divot contrast softens as time goes on, and so reaching a $c \sim 6$ (as we find) may only be a matter of the duration and collisional environment. Their divot has the more realistic form of a sharp transition to a negative slope, and then recovery to the post-divot slope. These two works present plausible explanations for the formation of a divot size distribution.

4.7 Future Work

In order to better constrain a divot in the "hot" objects' size distributions, new surveys are required. A survey covering a much larger area, and going as deep or deeper than CFEPS would be required to detect enough scattering

objects. The next best population to observe is the Plutinos, many of which have pericentres inside Neptune. Such a survey would need to go to a g-band magnitude past 25 in order to see a magnitude past the divot, which is what is necessary to have strong sensitivity to the divot. A survey which goes to 26th magnitude in g-band and covers hundreds of square degrees would be able to see the post-divot recovery in the Neptune Trojan population. A well characterised survey of the Centaurs (none exist, and so there is no well constrained size distribution) could potentially also measure the divot size distribution. A Centaur or JFC survey would be sensitive to small, close objects, and so be dominated by post-divot objects. It would be difficult to constrain the form across the divot with such a survey, though new large scale telescopes such as the Large Synoptic Survey Telescope may provide the scale needed.

The "cold" Kuiper Belt population is confined to semimajor axes between 42.5 and 44.5 AU (Petit et al., 2011). With eccentricities up to about 0.1, this population is confined to $q > 39$ AU. While it is not required that this population also has a divot at the same magnitude nor with the same contrast, having such a divot at $H_g = 9$ would mean a rough rollover magnitude around 26 in g-band. The shallowest luminosity function slopes (in apparent mag) that have been detected (at about 2 σ) in the literature (Fraser and Kavelaars, 2008; Fuentes and Holman, 2008) are "knee". A divot would be "smeared" to a "knee" when measured in apparent magnitudes; this observed "knee" may be a detection of a divot size distribution. Previous surveys should be re-examined in this light, but the best survey would be one that is wide enough to have at least 10 detections brighter than the limit, as well as one that extends to at least a magnitude after the limit.

While we test the sensitivity of our result to the placement of planets in the outer Solar System with GC06, the same analysis should be carried out for a model with planet migration in order to compare with the Nice model.

As stated, the "hotter" KRQ11 model improves the i match, but worsens the a match. Ongoing and future work includes exploring intermediate initial inclination distributions, with widths $5^\circ < \sigma_i < 12^\circ$. This will constrain the inclination distribution at the time of planetesimal formation.

Chapter 5

Summary and Conclusions

We present a measurement of a divot in the Kuiper Belt's scattering objects. Via joint analysis of the Canada France Ecliptic Plane Survey's scattering sample and the Kaib et al. (2011b) model, we constrain the form of the scattering objects' size distribution. We present a divot with a bright end slope of $\alpha_b = 0.8$ to $H_g = 9$ where it drops precipitously by a factor of ~ 6 and then recovers with a faint slope of $\alpha_f = 0.5$. Using this size distribution, and the absolute calibration of CFEPS, we estimate that there are $2 \cdot 10^6$ scattering objects with $H_g < 13$. Extrapolating the faint end slope to $H_g = 19$, we estimate there are $2 \cdot 10^9$ with $H_g < 18$, providing enough scattering objects for the production of the Jupiter Family Comets. We discuss our preferred divot scenario in the context of an implanted "hot" population, linking the scattering objects, Plutinos and Neptune Trojans. This is consistent with the observed size distributions for both populations and explains the previously thought "missing" intermediate-sized Neptune Trojans. Our scenario provides an integrated explanation for the "hot" populations of the outer Solar System and resolves several previously unsolved problems.

Bibliography

Becker, A. C., Arraki, K., Kaib, N. A., Wood-Vasey, W. M., Clocchiatti, A., Covarrubias, R., Damke, G., Davis, T. M., Filippenko, A. V., Foley, R. J., Garg, A., Garnavich, P. M., Hicken, M., Jha, S., Kirshner, R. P., Krisciunas, K., Leibundgut, B., Li, W., Matheson, T., Miceli, A., Miknaitis, G., Narayan, G., Pignata, G., Prieto, J. L., Rest, A., Riess, A. G., Salvo, M. E., Schmidt, B. P., Smith, R. C., Sollerman, J., Spyromilio, J., Stubbs, C. W., Suntzeff, N. B., Tonry, J. L., and Zenteno, A.: 2008, *Ap.J. (Letters),* **682**, L53

Bernstein, G. M., Trilling, D. E., Allen, R. L., Brown, M. E., Holman, M., and Malhotra, R.: 2004, *A.J.,* **128**, 1364

Bottke, W. F., Durda, D. D., Nesvorný, D., Jedicke, R., Morbidelli, A., Vokrouhlický, D., and Levison, H.: 2005, *Icarus* **175**, 111

Bottke, W. F., Morbidelli, A., Jedicke, R., Petit, J.-M., Levison, H. F., Michel, P., and Metcalfe, T. S.: 2002, *Icarus* **156**, 399

Brown, M. E.: 2001, *A.J.,* **121**, 2804

Campo Bagatin, A. and Benavidez, P. G.: 2012, *M.N.R.A.S.,* **423**, 1254

Chiang, E. I., Jordan, A. B., Millis, R. L., Buie, M. W., Wasserman, L. H., Elliot, J. L., Kern, S. D., Trilling, D. E., Meech, K. J., and Wagner, R. M.: 2003, *A.J.,* **126**, 430

Dohnanyi, J. S.: 1969, *Journal of Geophysical Research* **74**, 2531

Duncan, M., Quinn, T., and Tremaine, S.: 1987, *A.J.,* **94**, 1330

Duncan, M. J. and Levison, H. F.: 1997, *Science* **276**, 1670

Edgeworth, K. E.: 1943, *Journal of the British Astronomical Association* **53**, 181

Elliot, J. L., Kern, S. D., Clancy, K. B., Gulbis, A. A. S., Millis, R. L., Buie, M. W., Wasserman, L. H., Chiang, E. I., Jordan, A. B., Trilling, D. E., and Meech, K. J.: 2005, *A.J.,* **129**, 1117

Fernandez, J. A.: 1980, *M.N.R.A.S.,* **192**, 481

Fraser, W. C.: 2009, *Ap.J.,* **706**, 119

Fraser, W. C., Brown, M. E., and Schwamb, M. E.: 2010, *Icarus* **210**, 944

Fraser, W. C. and Kavelaars, J. J.: 2008, *Icarus* **198**, 452

Fraser, W. C. and Kavelaars, J. J.: 2009, *A.J.,* **137**, 72

Fuentes, C. I. and Holman, M. J.: 2008, *A.J.,* **136**, 83

Gladman, B.: 2005, *Science* **307**, 71

Gladman, B. and Chan, C.: 2006, *Ap.J. (Letters),* **643**, L135

Gladman, B., Lawler, S. M., Petit, J.-M., Kavelaars, J., Jones, R. L., Parker, J. W., Van Laerhoven, C., Nicholson, P., Rousselot, P., Bieryla, A., and Ashby, M. L. N.: 2012, *A.J.,* **144**, 23

Gladman, B., Marsden, B. G., and Vanlaerhoven, C.: 2008, *Nomenclature in the Outer Solar System*, pp 43–57

Gladman, B. J., Davis, D. R., Neese, C., Jedicke, R., Williams, G., Kavelaars, J. J., Petit, J.-M., Scholl, H., Holman, M., Warrington, B., Esquerdo, G., and Tricarico, P.: 2009, *Icarus* **202**, 104

Gomes, R., Levison, H. F., Tsiganis, K., and Morbidelli, A.: 2005, *Nature,* **435**, 466

Jedicke, R., Larsen, J., and Spahr, T.: 2002, *Aster* pp 71–87

Johansen, A., Oishi, J. S., Mac Low, M.-M., Klahr, H., Henning, T., and Youdin, A.: 2007, *Nature,* **448**, 1022

Kaib, N. A., Quinn, T., and Brasser, R.: 2011a, *A.J.,* **141**, 3

Kaib, N. A., Roškar, R., and Quinn, T.: 2011b, *Icarus* **215**, 491

Kavelaars, J.-J., Jones, R. L., Gladman, B. J., Petit, J.-M., and Parker, J. W.: 2008, *LPI Contributions* **1405**, 8378

Kenyon, S. J. and Bromley, B. C.: 2012, *A.J.,* **144**, 29

Levison, H. F. and Duncan, M. J.: 1997, *Icarus* **127**, 13

Morbidelli, A., Bottke, W. F., Nesvorný, D., and Levison, H. F.: 2009, *Icarus* **204**, 558

Morbidelli, A., Levison, H. F., Tsiganis, K., and Gomes, R.: 2005, *Nature,* **435**, 462

O'Brien, D. P. and Greenberg, R.: 2005, *Icarus* **178**, 179

Petit, J.-M., Kavelaars, J. J., Gladman, B. J., Jones, R. L., Parker, J. W., Van Laerhoven, C., Nicholson, P., Mars, G., Rousselot, P., Mousis, O., Marsden, B., Bieryla, A., Taylor, M., Ashby, M. L. N., Benavidez, P., Campo Bagatin, A., and Bernabeu, G.: 2011, *A.J.,* **142**, 131

Sheppard, S. S.: 2010, *A.J.,* **139**, 1394

Sheppard, S. S. and Trujillo, C. A.: 2006, *Science* **313**, 511

Sheppard, S. S. and Trujillo, C. A.: 2010, *Ap.J. (Letters),* **723**, L233

Solontoi, M., Ivezić, Ž., Jurić, M., Becker, A. C., Jones, L., West, A. A., Kent, S., Lupton, R. H., Claire, M., Knapp, G. R., Quinn, T., Gunn, J. E., and Schneider, D. P.: 2012, *Icarus* **218**, 571

Tancredi, G., Fernández, J. A., Rickman, H., and Licandro, J.: 2006, *Icarus* **182**, 527

Trujillo, C. A., Jewitt, D. C., and Luu, J. X.: 2000, *Ap.J. (Letters),* **529**, L103

Tsiganis, K., Gomes, R., Morbidelli, A., and Levison, H. F.: 2005, *Nature,* **435**, 459

Volk, K. and Malhotra, R.: 2008, *Ap.J.,* **687**, 714

Wolff, S., Dawson, R. I., and Murray-Clay, R. A.: 2012, *Ap.J.,* **746**, 171

Appendix A

Drawing From A Divot Distribution

Sample python code for drawing from a divot or "knee" Size distribution:

```
import numpy as np

random = np.random.random()

#The total number of objects to draw from the distribution
size=10**6

#The distribution parameters
slopeb=0.8 #bright slope
slopef=0.5 #faint slope
hb=1 # arbitrary bright end
hd=9.0 # divot/knee location
hs=13 # faint end  H value
c=10**(-0.75) #contrast value

#Determine the fraction in the bright distribution
cbt=1/(1+c*slopeb/slopes*(10**(slopef*(hs-hk))-1))

#Instantiate the H array
hmag=np.zeros(size)

#Draw from the bright and faint distributions
for i in range(0,size):

    if (random < cbt):
        slope=slopeb
        h0=hb
        h1=hd
```

```
        h0s10 = 10**(slope*h0)
        h1s10 = 10**(slope*h1)
        random=np.random.random()
        h = np.log10( random*(h1s10 - h0s10) + h0s10 ) / slope
    else:
        slope=slopef
        h0=hd
        h1=hs
        h0s10 = 10**(slope*h0)
        h1s10 = 10**(slope*h1)
        random=np.random.random()
        h = np.log10( random*(h1s10 - h0s10) + h0s10 ) / slope

    hmag[i]=h
```

Appendix B

Selecting Scattering Objects

A python script which separates scattering objects, given two different 10Myr time steps:

```
# This file determines if an object is scattering within the last
# 10 my based on the input from two files.
# Lo is the list of objects from the previous time step.
# f is the file containing the current time step to be checked for
# scattering objects
# out is the output file
#
# Written by Cory Shankman
# November 2011

import numpy as np
Lo = np.genfromtxt('q200_4-8_gy.dat')
f=open('q200_4-9_gy.dat','r')
out=open('q200_scattering.dat','w')

# Set the necessary scattering condition for the semi major axis in
# units of the input files
scattcon=1.5

# Iniitialize old id to an id value that does not exist
idold = 1

# Is scattering satisfied? Initially assumed to be no
cond=False

while (True):
    # Read the next line from the file to be checked
    line = f.readline()
    # If the size of the input is smaller than some number
```

```
# (10 is arbitrary), then the file has ended, so break the loop
if (len(line)<10):
    break

# This takes the input string, removes all blank space and stores
# the rest as a list of strings
Lt =line.rsplit()

# The id needs to be parsed as an int, and a (semi-major axis) as
# a float
id = int(Lt[0])
a = float(Lt[2])

# If the id is the same as the last time, perform the same action
# as before
if (id == idold):
    # If id is the same, and scattering condition held for, assume
    # scattering condition holds for all particles of same id
    if (cond == True):
        out.write(line)
    # If the scattering condition doesn't hold, don't write anything out.

# If this is a new id, have the check between the two files
else:
    # Find all lines in old time step where the id being checked exists
    exists = np.where(Lo[:,0]==id)

    # If it exists in any lines, do the following
    if (len(exists[0])>=1):
        # Set the row number to the first row where the match is found.
        # Again, assumes all particles of same id have same orbit
        row = exists[0][0]
# print id, Lo[row,0],  abs(a-Lo[row,2])
# This is a line to check to see if the scattering condition is being followed

        # If the change in a between the two time steps is greater than
        # the scattering condition
        if (abs(a-Lo[row,2])>scattcon):
            # set condition to true
            cond = True
```

```
            # write the line out to the output file
            out.write(line)
        else:
            # if not the scattering condition is not satisfied, set
            # the condition to false
            cond=False
    else:
        # If the object cannot be found in both files set the
        # scattering condition to false. Can happen if object goes
        # across q=200 threshold
        cond=False

# set idold to current id
idold=id
```